Sci. Dril., 34, 1–20, 2025
https://doi.org/10.5194/sd-34-1-2025


Scientific Drilling
Open Access



# Unearthing the climate history of the Atacama Desert in northern Chile – deep drilling in two clay pans of the Coastal Cordillera

**Volker Wennrich[1], Julia Diederich-Leicher[1], Bárbara Nataly Blanco-Arrué[2,a], Christoph Büttner[3], Stefan Buske[3], Eduardo Campos Sepulveda[4], Tibor Dunai[1], Jacob Feller[1], Emma Galego[1], Ascelina Hasberg[1], Niklas Leicher[1], Damián Alejandro López[1], Jorge Maldonado[5], Alicia Medialdea[6,7], Lukas Ninnemann[3,b], Russell Perryman[8], Juan Cristóbal Ríos-Contesse[4], Benedikt Ritter[1], Stephanie Scheidt[1], Barbara Vargas-Machuca[1], Pritam Yogeshwar[2,a], and Martin Melles[1]**

[1]Institute of Geology and Mineralogy, University of Cologne, 50674 Cologne, Germany
[2]Institute of Geophysics and Meteorology, University of Cologne, 50969 Cologne, Germany
[3]Institute of Geophysics and Geoinformatics, TU Bergakademie Freiberg, 09596 Freiberg, Germany
[4]Department of Geological Sciences, Universidad Católica del Norte, Antofagasta, Chile
[5]Superex S.A. Diamond and Sonic Drilling Group, Santiago, Chile
[6]Geographical Institute, University of Cologne, 50674 Cologne, Germany
[7]National Research Centre on Human Evolution (CENIEH), 09002 Burgos, Spain
[8]Comprobe, Borehole Imaging and Orientation Services, Santiago, Chile
[a]now at: Leibniz Institute for Applied Geophysics, 30655 Hanover, Germany
[b]now at: Center for Interdisciplinary Digital Sciences (CIDS), TUD Dresden University of Technology, 01069 Dresden, Germany

**Correspondence:** Volker Wennrich (volker.wennrich@uni-koeln.de)

Received: 19 December 2024 – Revised: 11 March 2025 – Accepted: 18 March 2025 – Published: 16 July 2025

**Abstract.** The Atacama Desert is one of the driest deserts on Earth, with a predominantly hyperarid climate since at least the Miocene. Geological evidence, however, indicates that this overall hyperaridity was repeatedly interrupted by wetter periods. Deep-time precipitation reconstructions of the Atacama Desert are limited by scarce and discontinuous sediment sequences, most of which received moisture from wetter regions outside the Atacama Desert. Longer archives of the precipitation history in the desert interior during the Neogene are unfortunately extremely rare.

The sediment records of two tectonically blocked endorheic basins (also known as clay pans) in the Coastal Cordillera of northern Chile may fill the gaps in the paleo-precipitation record of the Atacama Desert. Comprehensive investigations of both clay pans applied intensive geological and geophysical site surveys and deep-drilling operations with subsequent downhole logging. Short pilot cores of up to 6.2 m in length already showed highly variable sediment successions reflecting strong hydroclimatic fluctuations on glacial–interglacial timescales. Electromagnetic and seismic surveys yielded a three-layer structure in both basins consisting of the resistive basement overlain by a low-resistivity basal and a high-resistivity upper sediment unit with total sediment thicknesses of more than $\sim$100 and $\sim$160 m in the Playa Adamito Grande (PAG) and Paranal clay pans, respectively. Assuming similar sedimentation rates to those of the pilot cores, this would imply that the sediment records of both clay pans span several million years.

Lithological data and downhole-logging results of the deep-drilling operations reveal strong heterogeneities in the sediment composition that presumably can be traced back to major climatic and/or tectonic shifts in the catchments of the clay pans. Whereas the fine-grained sediments at the base of the PAG sequence suggest longer-lasting lacustrine sedimentation with enhanced evaporative episodes, the lower sediment unit in the core from the Paranal clay pan consists of fluvial conglomerates and sandstones. Both lacustrine and fluvial sediments indicate

less arid conditions in the central Atacama Desert than today. Separated by distinct lithological boundaries, the upper sediments in both clay pans show several similar sediment facies typical of alluvial-fan deposition, e.g., proximal mudflows and debris flows, sheetflood, and distal alluvial sediment flows, but also pedogenic calcium sulfates. The shift to a predominant alluvial-fan deposition, which is common after torrential rainfall in the Atacama Desert today, implies a general modification of the environmental conditions of the study areas.

These initial results already highlight the potential of the sediment records from the PAG and Paranal clay pans to provide unprecedented information on the Neogene precipitation history in the hyperarid core of the Atacama Desert.

## 1 Introduction

The Atacama Desert in northern Chile and southern Peru (Fig. 1) is assumed to be one of the driest deserts on Earth (Dunai et al., 2005; Evenstar et al., 2017; Ritter et al., 2018), with its hyperarid core today receiving less than 2 mm precipitation per year (Houston, 2006). The extreme aridity results from three major driving factors: (1) the long-term stable position of the Atacama Desert at the subsiding branch of the Hadley cell (Houston, 2006), (2) the rain-shadow effect of the Andes (e.g., Garreaud et al., 2010; Houston and Hartley, 2003; Rech et al., 2010), and (3) the temperature inversion over the coastal Pacific Ocean caused by the upwelling of cold Humboldt Current waters that effectively prohibit landward moisture transport (Garreaud et al., 2010, 2009). Arid conditions in the Atacama Desert likely date back to the Late Cretaceous (Hartley et al., 2005) or Oligocene (Dunai et al., 2005; Evenstar et al., 2017) but are assumed to be intensified since the Miocene (e.g., Amundson et al., 2012; Dunai et al., 2005; Evenstar et al., 2009; Rech et al., 2019). Upper Miocene to Pleistocene sedimentary records of the Central Depression, Andean Precordillera, and Altiplano (Bobst et al., 2001; Hartley and Chong, 2002; Pfeiffer et al., 2018; Pizarro et al., 2019; Ritter et al., 2019; Sáez et al., 2012; Baker et al., 2001; Fritz et al., 2004; Nunnery et al., 2019), however, indicate more severe variations in the intensity of the overall aridity in the Atacama Desert. On a shorter timescale, scarce sediment sequences, like paleo-wetland sequences and rodent middens from the central Atacama Desert and the Andean Precordillera, reflect vegetation shifts triggered by pulses of less arid climate conditions over the last approximately 50 kyr that are traced back to interhemispheric teleconnections, e.g., by variations in the intensity of the South American Summer Monsoon (e.g., Latorre et al., 2002; Maldonado et al., 2005; Quade et al., 2008; Sáez et al., 2016). Most of these records, however, received moisture via groundwater and surface water flows from higher altitudes in the Precordillera, which partly biases the local climate signal. Climate archives from the Coastal Cordillera, which are completely disconnected from Precordillera runoff and thus record only local precipitation signals, unfortunately, are very rare (Diederich et al., 2020; Ritter et al., 2019).

Here, we present initial results of site surveys and deep-drilling operations in two tectonically blocked endorheic basins, also known as clay pans, located in the Coastal Cordillera of northern Chile. The investigations were carried out within the framework of the Collaborative Research Centre (CRC) 1211 "Earth – Evolution at the Dry Limit", a multidisciplinary project that investigates the mutual interplay of biology and landscape evolution in extremely water-limited environments on geological timescales (Dunai et al., 2020). Clay pans are widespread in the Coastal Cordillera and fill terminal basins formed from ancient fluvial drainages by tectonic drainage displacement along fault scarps (Arens et al., 2024; Ritter et al., 2019; Diederich et al., 2020). During rare decadal to centennial intense rain events, the clay pans are fed episodically by runoff from adjacent alluvial fans and ephemeral streams that drain only smaller catchments within the Coastal Cordillera (Wennrich et al., 2024). These catchments receive neither groundwater nor surficial water from outside the Coastal Cordillera and thus are hydrologically disconnected from wetter areas in the Precordillera and Altiplano. The clay pan records could therefore be valuable archives of hydrological changes in the Atacama Desert's hyperarid core.

## 2 Site description

### 2.1 Playa Adamito Grande (PAG) clay pan

The PAG clay pan (21°32′S, 69°54′ W; 940 m altitude) is located in the driest part of the Atacama Desert, which receives mean precipitation of $< 1\,\mathrm{mm\,yr^{-1}}$ (Houston, 2006). The endorheic basin was formed by tectonic activity along the reverse Adamito Fault (also called the "Cerro Aguirre Fault"; González et al., 2021), resulting in a steep fault scarp to the north of the clay pan (Fig. 2a and b). The vertical offset at the scarp is up to 100–130 m and has blocked the outflow of the basin through a meandering paleo-drainage towards the north (Maksaev and Marinovic, 1980; Allmendinger and González, 2010; Ritter et al., 2018). The Adamito Fault is known to have been active since at least the Miocene (González et al., 2021). The visible extent of the PAG clay pan measures approximately 640 m (N–S) by 1000 m (W–E); the catchment area comprises 560 $\mathrm{km^2}$ (red polygon in

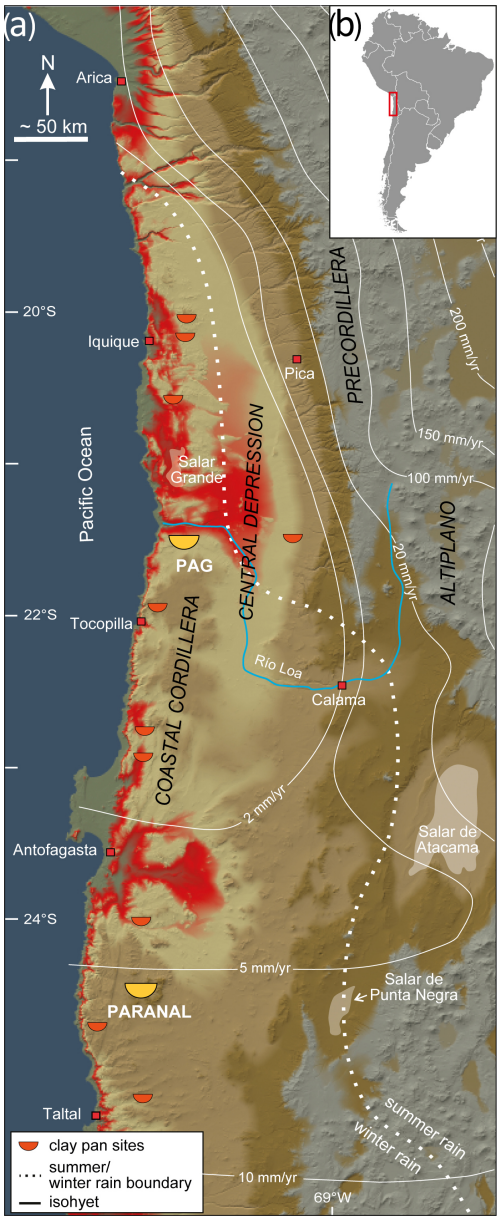


**Figure 1.** **(a)** Color-shaded digital elevation model of the Atacama Desert (derived from Shuttle Radar Topography Mission (SRMT) data and modified after Ritter et al., 2018) showing the locations of the Paranal and PAG clay pans (yellow half circles) as well as other clay pans in the Coastal Cordillera (orange half circles). The solid white lines highlight isohyets and the dotted line the border between winter-rain- and summer-rain-dominated areas (after Houston, 2006). **(b)** Location of the study area (red rectangle) in South America.

Fig. 2a) and is drained through small incised inlets from the east, southeast, and southwest, including the topographic high of Cerro de la Mica (1817 m altitude, Ritter et al., 2018, 2019; Fig. 2a). Basement rocks in the catchment are composed of Devonian sandstones and Jurassic volcanoclastic sequences as well as Early Cretaceous diorites, granodiorites, and andesitic porphyry (Harrington, 1961; Maksaev and Marinovic, 1980; Coira et al., 1982). In large parts of the basin, these basement rocks are covered by Neogene alluvial-fan deposits (Maksaev and Marinovic, 1980). Today, the clay pan area is barren of vascular plants. During our fieldwork, we only found sparse lichens macroscopically visible at the fault scarp north of the clay pan.

### 2.2 Paranal clay pan

The Paranal clay pan (24°29′ S, 70°09′ W; 2231 m altitude) is located in the eastern Pampa Remiendos as part of the Coastal Cordillera (Fig. 2c). The area receives mean precipitation of approximately 5 mm $yr^{-1}$, mainly in the form of small-amplitude rain events that primarily occur during the austral winter season (Houston, 2006; Reyers et al., 2021). The endorheic basin was formed by tectonic blocking of an ESE–WNW-oriented paleo-channel system, which formerly drained the Sierra Vicuña Mackenna mountain range towards the Pacific Ocean, along a trace of the Quebrada Grande Fault System as part of the Atacama Fault System (AFS; Herve, 1987; Scheuber and Andriessen, 1990; Blanco-Arrué et al., 2022; Fig. 2c). The tectonic activity in this segment of the AFS is dated to the Middle to Upper Miocene (19 to 5.5 Ma; Herve, 1987). The timing of the tectonic pulse that caused the final blockage of the clay pan, however, is still unknown. Today, the clay pan forms a terminal basin that is fed episodically by surface runoff from adjacent alluvial fans and ephemeral streams. The catchment amounts to 170.8 $km^2$ and is defined by the up to 3114 m high Sierra Vicuña Mackenna to the northeast, east, and southeast (red polygon in Fig. 2c). Whereas the surrounding hills and mountains are built of Jurassic and Early Cretaceous dioritic to granodioritic plutonic rocks, the playa itself is located in Upper Miocene to Pleistocene alluvial to colluvial strata (Álvarez et al., 2016; Domagala et al., 2016). Most parts of the catchment and the surrounding mountains are barren of vegetation. Only a few perennial species, like *Adesmia atacamensis*, *Calandrinia salsoloides*, *Cistanthe arancioana*, *Nolana sessiflora*, and *Cryptantha* sp., are adapted to the harsh environment and colonize niches along fluvial channels and rocky outcrops as well as the flanks of higher mountains (Díaz et al., 2012; Elgueta and Barría, 2008).

## 3 Pre-site surveys

To evaluate the potential of the sedimentary records in the PAG and Paranal clay pans as suitable paleoclimate archives and to select the best targets for deep-drilling operations, comprehensive site surveys including cosmogenic nuclide exposure (CNE) dating and pilot coring were conducted during several field campaigns between 2013 and 2015.

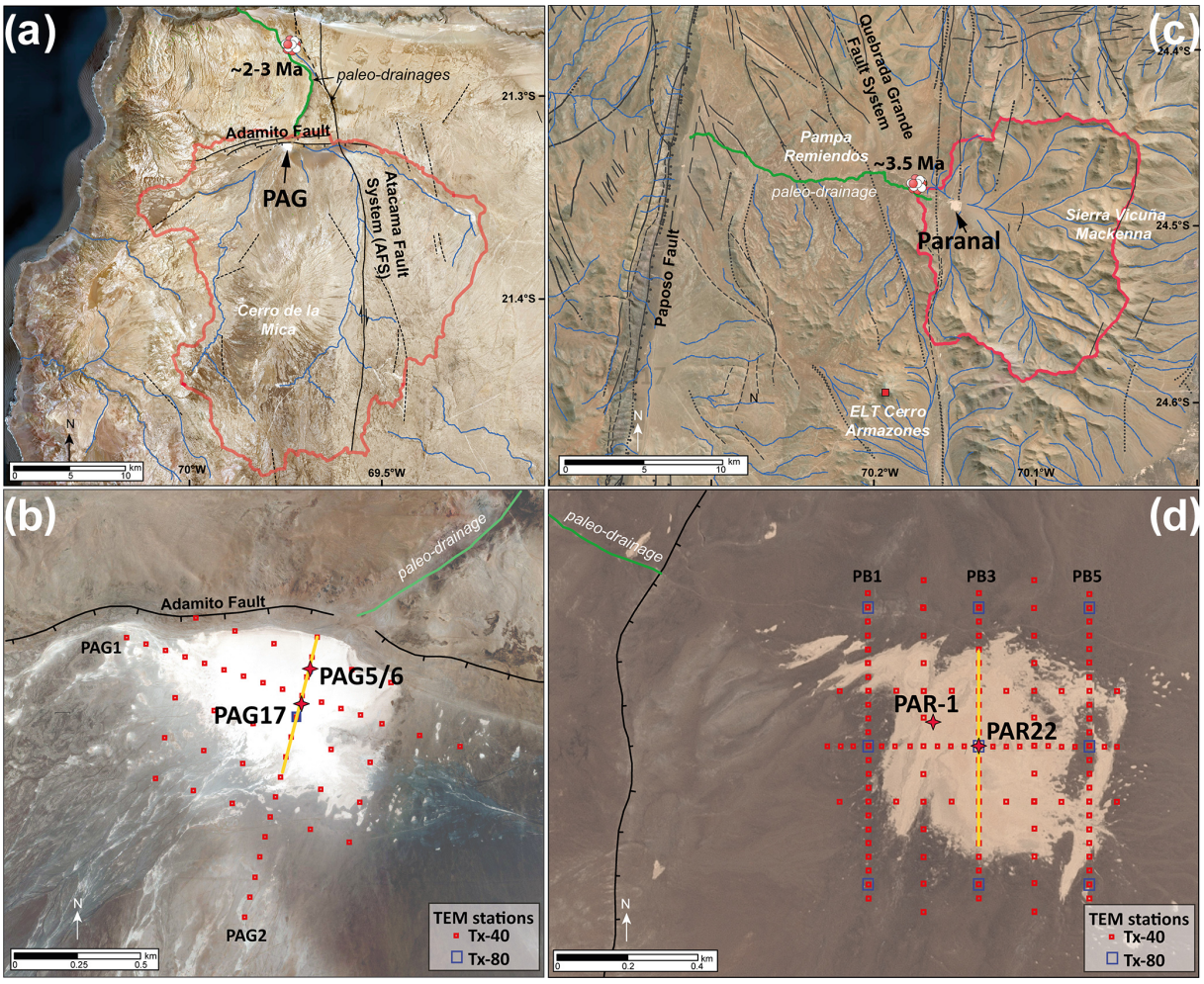


**Figure 2.** Maps of the studied clay pans in the Coastal Cordillera. **(a)** Satellite imagery of the PAG area (derived from Sentinel data) with the clay pan's catchment (red polygon) and major inlets (blue lines). Solid, dashed, and dotted black lines highlight faults after Maksaev and Marinovic (1980). The icon marks the position of a cosmogenic nuclide exposure (CNE) sample from the paleo-drainage (Ritter et al., 2018). **(b)** Close-up of the PAG clay pan (Sentinel-1B imagery) with the Adamito Fault (black line) and the paleo-drainage (green line) to the north of the clay pan. The sites of the PAG5/6 pilot core and PAG17 deep drilling (red stars), the transient electromagnetic (TEM) stations (red squares), and the N–S seismic profile presented in Fig. 3b (yellow line) are indicated. **(c)** Satellite image of the Paranal clay pan in the Pampa Remiendos with its catchment (red polygon) and major tributaries (blue lines) derived from the TandemX DEM. The green line marks the course of the paleo-drainage and the icon the position of a CNE sample from the abandoned paleo-channel. Solid, dashed, and dotted black lines highlight observed, inferred, and covered faults, respectively (modified after Álvarez et al., 2016; Domagala et al., 2016). **(d)** Close-up of the Paranal clay pan (SPOT7 multispectral (MS) imagery) showing the fault scarp and blocked paleo-drainage to the west of the clay pan as well as the locations of the PAR-1 pilot coring and PAR22 deep-drilling sites along with the position of the TEM soundings (red squares) and the N–S seismic profile presented in Fig. 3d (yellow line).

### 3.1 CNE dating

CNE dating was employed to date the most recent fluvial activity in the paleo-drainages of the clay pans prior to their final drainage cutoffs due to tectonic activity. Thereby, CNE dating can provide minimum age constraints for the formation of the clay pans. For that purpose, fluvially rounded quartz pebbles were collected from the abandoned outflow channels of both clay pans (Fig. 2a, c). Samples from PAG were dated using $^{21}$Ne at the Scottish Universities Environmental Research Centre (SUERC; for details, see Ritter et al., 2018), while the Paranal samples were measured at the University of Cologne after Ritter et al. (2021) using the identical input parameters for the calculation of the exposure ages as in Ritter et al. (2018).

In the paleo-drainage of the PAG clay pan, $^{21}$Ne exposure ages cluster at ∼ 8 and ∼ 2–3 Ma (Ritter et al., 2018). The $^{21}$Ne exposure ages of clasts from the paleo-drainage of the Paranal clay pan reveal a more distinct cluster at $3.5 \pm 0.24$ Ma ($n = 3$) and two Miocene ages ($7.66 \pm 0.28$

and $10.96 \pm 0.49$ Ma). These results imply that both paleodrainages finally became abandoned some time during the Middle to Late Pliocene.

### 3.2 Pilot coring

In 2014 and 2015, first exploratory sediment cores were recovered from the PAG and Paranal clay pans using a handheld percussion-drilling system (Eijkelkamp, the Netherlands). The cores were investigated using multiproxy approaches.

Core PAG5/6 originates from the northern central part of the PAG clay pan (Fig. 2b) and has a total length of 6.2 m. Luminescence and paleomagnetic dating suggest that the record spans at least the last 215 kyr (Ritter et al., 2019). The sediments of core PAG5/6 show a strongly heterogeneous composition, with coarse-grained (sand and gravel) deposits in the lower core section suggesting higher fluvial (alluvial) input into the basin during Marine Isotope Stage (MIS) 7 to MIS 5 (Ritter et al., 2019). Finer sediments towards the top were linked to a progressive reduction in the inflow from MIS 4 to MIS 1, with only a few interspersed coarse layers indicating irregularly occurring intense flooding events. Overall, variations in sedimentological, geochemical, sediment-physical, and biological proxies along the core imply that the long-term hyperaridity in the area witnessed small but significant precipitation changes with several pluvial phases since the penultimate interglacial. These precipitation changes are assumed to be linked to variations in the Pacific Ocean sea surface temperature in glacial–interglacial cycles (Ritter et al., 2019).

Core PAR-1 was retrieved from the western part of the Paranal clay pan (Fig. 2d) and has a length of 1.88 m. Although the chronology of the core is relatively poorly constrained, sparse reliable radiocarbon and luminescence dates imply that the sediments were deposited since the Late Pleistocene after $\sim 32$ ka (Wennrich et al., 2024).

To elucidate its paleoenvironmental information, investigations of the core composition were combined with a modern ground-truthing approach based on historic rain events since 1990, which combines sediment data with remote sensing, meteorological, and climate-modeling data. The results indicate that today significant surface runoff in the Paranal catchment and subsequent water and sediment inflow into the clay pan are limited to infrequent ENSO-related heavy rains $> 20$ mm, which occur in the area with a mean recurrence rate of 6 years. Distal overland flows or mudflows triggered by these heavy rains dominate the Holocene part of the record and are thus regarded as primary sedimentological processes. In addition, however, more coarse-grained, well-sorted sediment layers are intercalated in the Holocene sediments at a mean frequency of 1070–1430 years, which represent stronger millennial-scale flood events that exceed the historical observations in amplitude. The sediments formed during the Late Pleistocene, in contrast, predominantly consist of even coarser sediments, which were likely deposited by proximal mudflow or debris-flow events. This reflects widespread wetter conditions in the southern Atacama Desert than today during the Late Pleistocene CAPE (Central Atacama Pluvial Events; Quade et al., 2008; Sáez et al., 2016).

## 4 Geophysical survey and site selection

To investigate the thickness and architecture of the sedimentary strata of the PAG and Paranal clay pans as well as the bedrock topography, comprehensive geophysical site surveys using transient electromagnetic (TEM) and active seismic methods were carried out in October 2018 and December 2019.

The TEM surveys applied a central loop configuration with transmitter loop sizes of $40\,\text{m} \times 40\,\text{m}$ (Tx-40) and $80\,\text{m} \times 80\,\text{m}$ (Tx-80) with an inner $10\,\text{m} \times 10\,\text{m}$ receiver loop covering the entire clay pan areas on a 3D grid (Fig. 2b and d) using the ABEM Walk TEM system (Guideline Geo AB, Sweden). A total of 56 TEM soundings was recorded at the PAG clay pan (Fig. 2b), whereas 116 soundings were recorded at the Paranal clay pan (Fig. 2d; Blanco-Arrué et al., 2022). The acquired TEM data were processed using a robust stacking scheme to yield high-quality transients (Blanco Arrué, 2024). Postprocessing analyses involved conventional 1D Marquardt–Levenberg (ML) and Occam inversion methods (e.g., Yogeshwar et al., 2020) in order to develop both minimum-layered models with sharp interfaces and smooth models, respectively. Both techniques result in a credible 1D electrical resistivity model at each sounding location. A spatial visualization of the sediment distribution and the bedrock topography is derived from the 1D resistivity models.

The TEM surveys were complemented by seismic refraction surveys of both clay pans in order to obtain *P*-wave velocity models that provide increased spatial resolution for imaging the shallow subsurface sedimentary infills. Data acquisition was conducted using vertical-component geophones as receivers and an accelerated weight drop with a mass of $\sim 40$ kg attached to a pickup truck as the seismic source. The weight drop was preferred to a conventional sledgehammer source due to its higher emitted energy. The receiver point distance was 2 m for the whole profile. The source point distance was 4 m at the ends of the profiles and decreased to 2 m at the centers to increase the spatial resolution at shallow depths in these areas. For the PAG basin, a N–S profile was recorded using 140 source points and a fixed spread of 288 receivers (geophones). This results in a profile length of about 576 m. In the case of the Paranal basin, seismic recordings were conducted along a N–S profile spanning most of the visible extent of the clay pan. Altogether, 288 geophones were deployed, resulting in a profile length of approximately 576 m.

### 4.1 PAG clay pan

At the PAG site, the derived TEM resistivity models exhibit spatially consistent variations and indicate a three-layer subsurface structure with an electrical conductive layer between two resistive layers (Fig. 3a). The deep resistive layer exhibits resistivities of more than 300 Ωm and can be resolved to a maximum depth of ∼ 300 m. Due to its high resistivity and uniformity within the basin, we interpret the layer as the local bedrock. With a sharp resistivity contrast, the presumed bedrock is overlain by a conductive body of ∼ 3 Ωm. Due to its lenticular geometry with a maximum thickness of ∼ 70 m in the basin center and its thinning towards the edges with low slope angles (below ∼ 5°; Fig. 3a), the conductor is regarded as the basal sediment infill. The extent of the sediment infill significantly exceeds the visible surface area of the modern clay pan. The uppermost shallow resistive layer has resistivity values between 80 and 200 Ωm and forms a rather uniform tabular geometry across the basin with an average thickness of ∼ 30 m. Assuming that the lower resistive layer reflects the bedrock, an estimated maximum sediment thickness of 103 ± 10 m is observed towards the northern edge of the basin. The location coincides with the head of the paleochannel, which is assumed to have been the major drainage of the basin, right before the uplift along the Adamito Fault (Fig. 3a).

*P*-wave velocity information was obtained by first-arrival travel-time tomography to a depth of approximately 30–40 m (Fig. 3b) given the present velocity distribution and the limited profile length. Seismic velocities below 20 m are comparably high, reaching values of ∼ 1700–2000 m s$^{-1}$. Above 20 m, the *p*-wave velocities decrease gradually, first to ∼ 1500–1000 m s$^{-1}$ and then, above 10 m, to ∼ 1000–400 m s$^{-1}$. This finding is consistent with *P*-wave velocities observed in the Huara clay pan located approximately 200 km to the north of PAG (Fig. 1a; Diederich et al., 2020). The most dominant velocity contrast is visible at roughly 30 m depth, as depicted by the black contour line marking the highest 5 % ray coverage in Fig. 3b. The depth of this prominent seismic refractor fits well with the shallow transition from resistive to conductive sediments, indicating a distinct change in the sedimentary composition. The depth of the refractor trends to larger depths towards the northern edge of the clay pan (Fig. 3b) suggests a slightly asymmetrical geometry of the sediment infill that is likely to be linked to tectonic uplift along the Adamito Fault.

### 4.2 Paranal clay pan

In the Paranal clay pan, the 1D models of the TEM data provide information down to ∼ 250 m (Blanco-Arrué et al., 2022). As can be seen, for instance, in transects PB1, PB3, and PB5, the resistivity models exhibit a three-layer structure (Fig. 3c), similar to the PAG clay pan. The lower resistive layer at Paranal exhibits resistivities of ∼ 200 Ωm and is interpreted as the local dioritic to granodioritic bedrock. The bedrock is overlain by a conductive layer of ∼ 20 Ωm, with varying thicknesses from ∼ 20 m on the northern periphery to ∼ 110 m in the center of the clay pan. The transition from the bedrock to the conductive layer indicates a channel-like geometry that is oriented in E–W, with slope angles of roughly 20° along the northern and southern edges. The structure is interpreted as a channel of a paleo-river that incised down to approximately 80 m in the underlying basement rocks (Blanco-Arrué et al., 2022) and presumably belongs to the paleo-drainage that drained the Sierra Vicuña Mackenna towards the Pacific Ocean (Herve, 1987; Scheuber and Andriessen, 1990). At a depth of ∼ 50 m, the conductive strata are overlain by a layer of higher resistivity (> 100 Ωm). Due to differences in the thickness of the conductive layer, the presumed total sediment thickness in Paranal is rather heterogeneous, ranging from 100 ± 10 m at the edges to 160 ± 10 m in the center of the postulated paleo-channel.

The seismic data along the N–S-oriented profile yield information down to roughly 70 m (Fig. 3d), which is insufficient to resolve the basement contact derived from the TEM models. In the lower part of the seismic profile, the deposits are characterized by high velocities > 2000 m s$^{-1}$, which are in the range of semi-consolidated clastic sediments in the Pampa del Tamarugal (Labbé et al., 2018). At about 50 m depth, however, the *P*-wave velocities quickly decrease to < 1800 m s$^{-1}$. This finding and the high ray coverage (as indicated by the contour line of the 7 % highest ray coverage in Fig. 3d) imply a significant seismic refractor at 50 m depth, which is consistent with the transition from the conductive to the overlying resistive layers resolved by the TEM data. Along the seismic profile, the refractor indicates a rather heterogeneous shape and appears to be discontinuous in the central part (Fig. 3d), where the TEM data image the paleochannel. In this zone, another refractor is indicated at approximately 60 m in depth. The greater lateral extent, however, is not resolved due to the limited profile length. Between approximately 50 and 30 m, velocities gradually drop from approximately 1800 to 1000 m s$^{-1}$, without a clear refractor. Velocities in the uppermost 30 m are relatively homogenous at < 1000 m s$^{-1}$ and are only slightly elevated at ∼ 10 m depth, where a higher ray coverage (Fig. 3d) points to another shallow refractor. In contrast to the lower two refractors, the upper one exhibits a rather uniform shape extending all along the N–S profile.

## 5 Deep-drilling operations and downhole logging

The PAG17 and PAR22 deep-drilling campaigns took place in October 2017 and January/February 2022, respectively. Both drillings were operated by SUPEREX S.A., a Chilean drilling company. Most of the drilling was performed using a truck-mounted SDC 550 sonic-drilling rig (Sonic Drill Corp.; Canada; Fig. 4a) with 1.5 m split-core barrels (4.5 in.

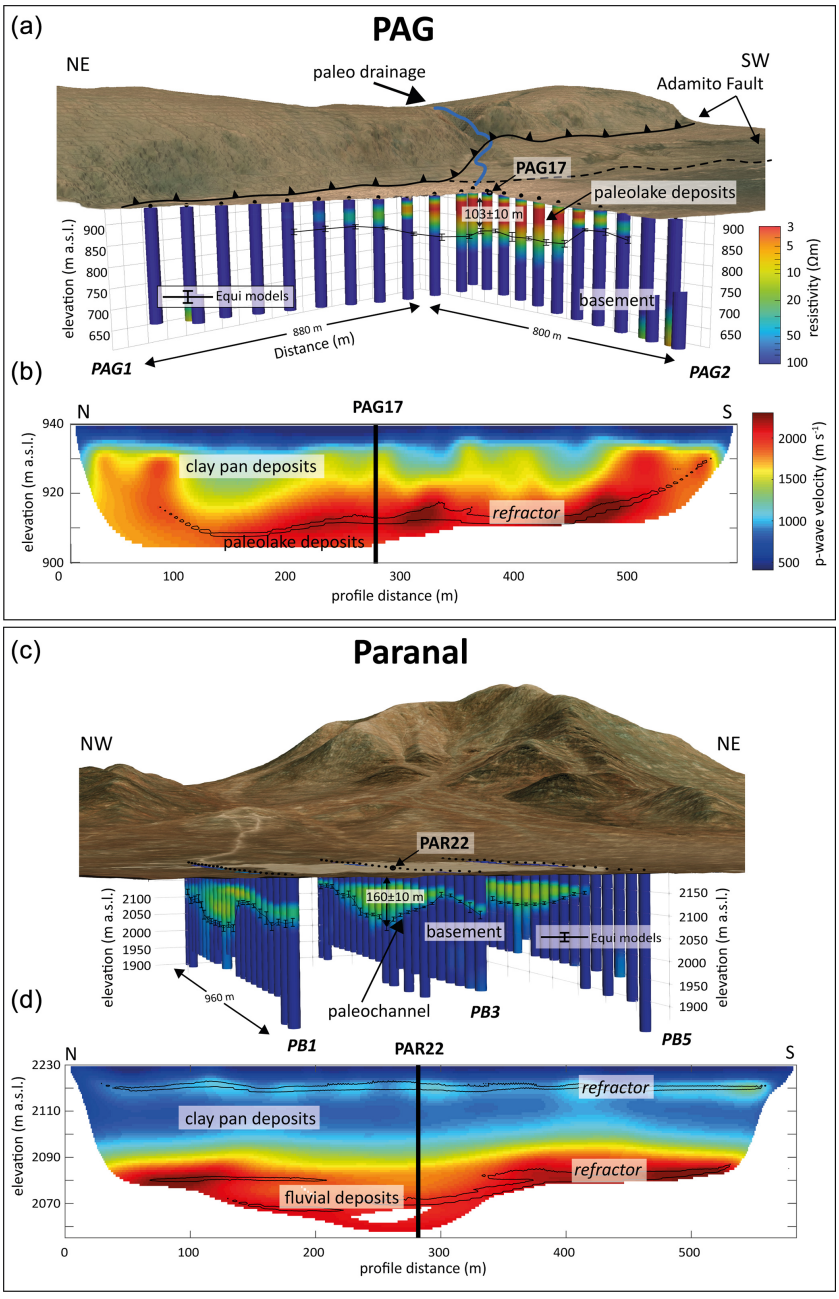


**Figure 3.** Results of the geophysical surveys in the PAG **(a, b)** and Paranal **(c, d)** clay pans. **(a, c)** Three-dimensional view of the PAG **(a)** and Paranal **(c)** clay pans with the 1D-stitched inversion results using Occam 1D models for the PAG-1 and PAG-2 transects as well as the PB1, PB3, and PB5 transects, respectively (see Fig. 2b and d for the positions of the profiles). Black dots illustrate the TEM stations on the surface of the clay pan. The ranges of the estimated basement depths obtained by the equivalent models are displayed as error bars. The satellite image was obtained from ESRI satellite imagery (2021). All TEM 1D models are shown up to the depth of investigation. The elevation is shown with double vertical exaggeration. **(b, d)** *P*-wave velocity models along two north–south profiles across the PAG **(b)** and Paranal **(d)** clay pans. Overlain black contour lines mark areas with the highest 5 % (PAG) and 7 % (Paranal) ray coverages.

H90 RH) and a 6 or 7 in. HPS sonic casing (both Hole Products; USA). The sonic drilling is operated without cooling liquids (Barrow, 1994), making this technique especially valuable for remote desert environments. The sediment cores were recovered in clear (PAG17) or opaque (PAR22) Lexan core liners (inner diameter 88.9 mm). During the lowering of the casing, compressed air was injected into the drill head to blow out fine dust trapped between the drill string and the casing to reduce friction. For the lowermost coarse-grained strata of the Paranal clay pan, the technique was changed


**Figure 4.** Field images of **(a)** the PAG17 site with the sonic drilling rig SDC 550 (white truck), the auxiliary truck (red), and the core processing tent (front) setup (picture: Jan Voelkel). **(b)** The PAR22 drill site with the diamond drilling rig (left), the auxiliary truck (center), and the core processing tent (right).

to HQ diamond (rotary) drilling, which was performed with a truck-mounted drilling rig and an HQ3 diamond drill bit (Fig. 4b).

In the PAG clay pan, the drilling operation was conducted in the central part (PAG17; Figs. 2b and 4a), where the geophysical data indicate a maximum sediment thickness of up to ∼ 100 m (Fig. 3a). Altogether, four holes (PAG17-1A to PAG17-1D) were drilled approximately 2 m apart from each other down to maximum depths of 7.5, 31.0, 51.0, and 17.1 m, respectively (Table 1). Due to technical issues, the drilling had to be stopped at a depth of 51.0 m so that the lowermost ∼ 50 m of the sediment record expected from the geophysical site survey (103 ± 10 m) remained undrilled. The recovery of hole PAG17-1A was 94.5 % (Table 1). Core loss was mainly due to partial melting of the Lexan liners as a result of dust-induced friction between the casing and the drill string. After applying compressed air, the recovery increased to 95.1 %, 119.5 %, and 100 % for holes PAG17-1B, PAG17-1C, and PAG17-1D, respectively (Table 1). Recoveries > 100 % are explained by sediment expansion during the sonic drilling and/or backfall during the lifting and lowering of the drill string.

During the PAG17 campaign, natural gamma radiation (NGR) downhole logging was carried out in 10 mm steps using a portable gamma-ray acquisition system including a NGR slim-hole probe and the ALADIN Interface Panel (Antares Datasysteme GmbH, Germany). After finalizing the drilling operation and removal of the steel casing, holes PAG17-1A, PAG17-1B, and PAG17-1D were logged down to the bottom. Hole C, in contrast, was logged separately in the lower part (51.6–29.0 m) and the upper part (29.0–0 m) after sequential removal of the steel casing to prevent hole collapse while acquiring the full sequence without interferences from the steel rods.

For the PAR22 drilling operation, three holes (PAR22-1A to PAR22-1C) were cored at a distance of ∼ 10 m from each other in the center of the Paranal clay pan (Fig. 4b), where a maximum sediment thickness of 160 ± 10 m was expected from the geophysical site surveys (Blanco-Arrué et al., 2022; Fig. 3c). Holes PAR22-1A and PAR22-1B were drilled by sonic drilling down to depths of 32.8 and 52.3 m, respectively. In the case of hole PAR22-1A, the drill string got lost due to a twist-off, whereas a massive cobble layer hindered further penetration at PAR22-1B. The core recovery was 95.9 % for hole PAR22-1A due to partial melting of the Lexan liners, but increased to 124 % for hole PAR22-1B after applying the air compressor. Below 52.3 m, core PAR22-1B could be continued down to the basal depth of 174.0 m with 102.9 % core recovery using HQ3 (rotary) diamond drilling (Fig. 4b). Diamond drilling of hole PAR22-1C finally duplicated the depth interval between 48.0 and 100.5 m.

Downhole logging of the open PAR22 drill holes was performed at 1 cm resolution in March 2022, a few weeks after the drilling operations, by the Chilean company COMPROBE. Three different probes for spectral gamma radiation (SGR; QL40-SGR; Mount Sopris Instrument Co. Inc; USA), magnetic susceptibility (MS; HMI-453, W&R instruments, Czechia), and LS and SS inductive conductivity (Dual Induction probe DIL38; LIM SAS; France) were employed using a truck-mounted winch (Century Geophysical Corp.; USA; Fig. 5). Due to partial wall collapse, holes PAR22-1A; PAR22-1B, and PAR22-1C could only be logged down to depths of approximately 24.5, 134.5, and 94.5 m, respectively.

## 6 Preliminary drilling and downhole-logging results

### 6.1 PAG clay pan (PAG17)

The PAG17 cores mainly consist of unconsolidated clastic sediment particles along with calcium sulfate but lack visible organic matter compounds as well as traces of carbonate and salt. Based on the visual lithological description and NGR variations in the four boreholes, the PAG17 core composite was constructed and divided into seven facies (PAG-1 to PAG-7) that reflect different depositional and environmental conditions (Fig. 6a).

**Table 1.** Drilling technique, penetration, and core recovery of the drilling campaigns in the PAG and Paranal clay pans in 2017 and 2022, respectively, together with the used downhole-logging probes and the maximum logging depths. NGR – natural gamma radiation; SGR – spectral gamma radiation; MS – magnetic susceptibility; COND – inductive conductivity.

| Campaign | Drilling | Hole | From (m) | To (m) | Cored (m) | Recovery (%) | Downhole-logging probes | Maximum logging depth |
|---|---|---|---|---|---|---|---|---|
| PAG17 | Sonic | 1A | 0.0 | 7.5 | 7.5 | 94.5 | NGR | 4.2 |
| | Sonic | 1B | 7.5 | 31.0 | 23.5 | 95.1 | NGR | 31.3 |
| | Sonic | 1C | 0.0 | 51.0 | 51.0 | 119.5 | NGR | 29.0/51.6 |
| | Sonic | 1D | 0.0 | 17.1 | 17.1 | 100.0 | NGR | 17.1 |
| | | | | Total | 99.1 | 109.0 | | |
| PAR22 | Sonic | 1A | 0.0 | 32.8 | 32.8 | 95.9 | SGR, MS, COND | 24.5 |
| | Sonic | 1B | 0.0 | 52.3 | 52.3 | 124.2 | | |
| | Diamond | 1B | 52.3 | 174.0 | 121.7 | 102.9 | SGR, MS, COND | 134.5 |
| | Diamond | 1C | 48.0 | 100.5 | 51.0 | 105.0 | SGR, MS, COND | 94.5 |
| | | | | Total | 259.3 | 106.1 | | |

**Figure 5.** Downhole logging of hole PAR22-1C after the PAR22 deep drilling in the Paranal clay pan using a truck-mounted winch system.

### 6.1.1 Facies PAG-1: clastic playa lake deposits

Facies PAG-1 describes most of the sediments in the core interval from ∼51.7 to 30.4 mcd (meters composite depth). It consists of reddish-brown and massive clay to silt (Fig. 6j) with little sand and very few interspersed gravel grains in increasing abundance upwards. Facies PAG-1 is reflected by rather high NGR values of 100–120 API units (Fig. 6b). A certain water content of the overall fine-grained deposits likely explains their low resistivity in the TEM profiles (Fig. 3a).

The overall very low admixed sand content in facies PAG-1 argues against an eolian origin or sediment supply by mudflows. The fine grain size rather implies a relatively low-energy deposition in a larger water body, likely in a playa lake environment (Nalpas et al., 2008). Horizons with slightly enriched sand content within facies PAG-1 can be associated with periods of higher-energy fluvial supply into the playa lake during sporadic heavy-rain events, whereas the gradual increase in the gravel content upwards may be associated with increasing proximity to the shoreline during deposition.

### 6.1.2 Facies PAG-2: evaporitic playa lake deposits

The clastic sediments of facies PAG-1 are irregularly intercalated with millimeter- to centimeter-sized calcium-sulfate (gypsum or anhydrite) concretions, veins, and layers of facies PAG-2 (Fig. 6h, i). This facies is reflected in the somewhat reduced NGR values of 40–100 API units (Fig. 6b) and an elevated ion concentration, as indicated by the occurrence of calcium sulfates, which matches the low resistivity in the TEM profiles (Fig. 3a).

Like facies PAG-1, the deposition of facies PAG-2 can be traced back to a playa lake environment. The calcium-sulfate layers might be formed by precipitation from brine waters, like in modern Salar de Llamara (Criado-Reyes et al., 2023), or by evaporation of groundwater, as in the marginal zones of today's Salar de Atacama (Bobst et al., 2001). The lack of distinct erosional surfaces within facies PAG-1 and PAG-2, however, argues against longer-lasting subaerial exposure due to complete desiccation of the playa lake and thus indicates rather stable and persistent depositional conditions with cyclic fluctuations in ion concentrations, i.e., the salinity of the lake water.

### 6.1.3 Facies PAG-3: paleo-surface

Facies PAG-3 (30.4–29.2 mcd) is primarily composed of reddish-brown fine-grained deposits with only traces of calcium sulfate. It mainly differs from facies PAG-1 in its much

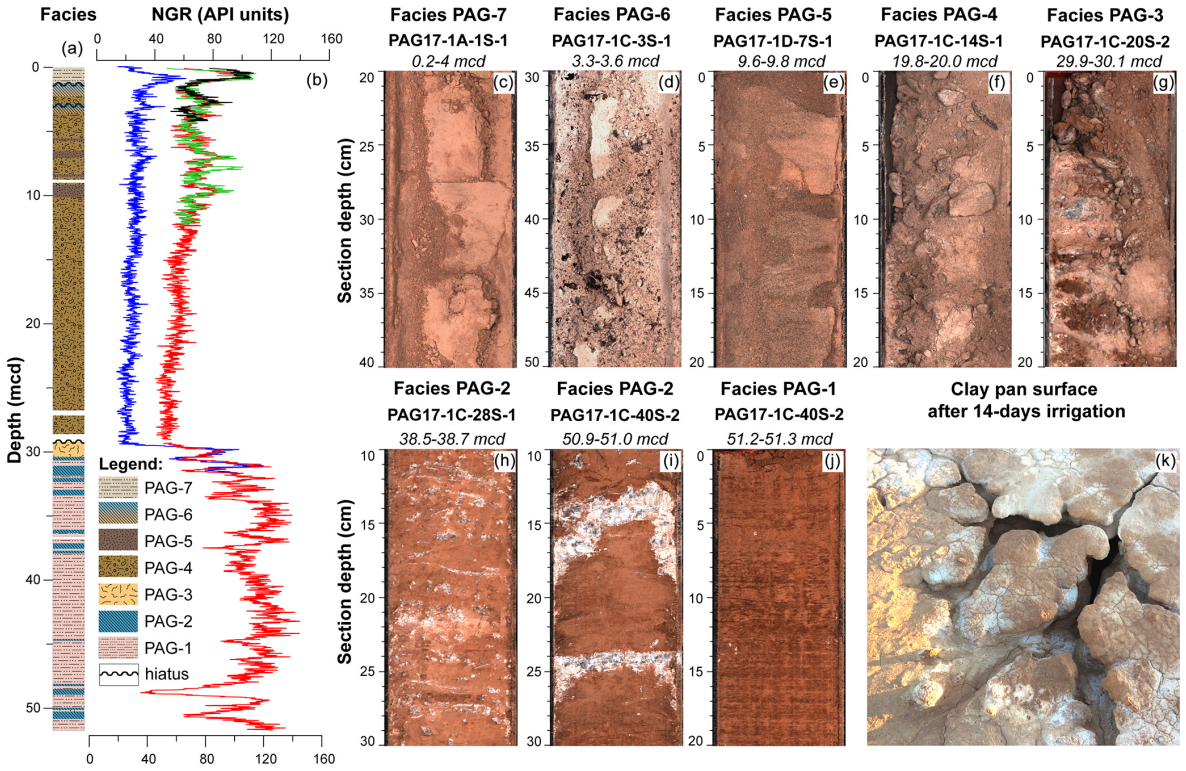


**Figure 6.** Initial results from the drilling and downhole logging at site PAG17 in the PAG clay pan, showing **(a)** the sedimentary facies of the core composite next to **(b)** the natural gamma radiation (NGR) in holes PAG17-1A (black), PAG17-1B (blue), PAG17-1C (red), and PAG17-1D (green). The photographs in panels **(c)**–**(j)** illustrate the different facies found in the PAG17 record, and panel **(k)** shows the modern clay pan surface after 14 d of irrigation.

higher content of sand and gravel-sized clasts, which explains the significant drop in NGR values down to ∼ 50 API units (Fig. 6b). Gravel is partly mixed into the fine-grained matrix but occurs much more prominently along an approximately 1 m-long feature that is aligned perpendicularly to the bedding of the fine-grained matrix and widens towards the top of the unit (Fig. 6g). This feature is interpreted as a desiccation crack that formed due to cyclic thermal contraction, swelling and shrinking of clay minerals (Sager et al., 2021), and/or partial dissolution of calcium sulfates during long-term subaerial surface exposure. Similar sand-filled cracks are common in the Atacama Desert (e.g., Owen et al., 2013), but, unlike gypsum and sand wedges (e.g., Sager et al., 2021; Zinelabedin et al., 2025), the crack in facies PAG-3 does not show any signs of cementation or growth patterns but rather contains loose and poorly sorted clastic material.

The widening of such desiccation cracks could be observed during a 14 d irrigation experiment of the PAG clay pan surface conducted during the drilling operation in 2017. The repeated irrigation of the surface resulted in the outwash of finer particles along preferential polygonal directions and a downward opening of the cracks (Fig. 6k). Once such a crack reaches a certain width, it can effectively trap eolian and fluvial sand and gravel. The formation of similar fossilized desiccation cracks in the Atacama Desert is often linked to initial pedogenesis, which, however, requires longer-term subaerial conditions during a non-depositional phase (Jordan et al., 2014; Rech et al., 2019). In the case of facies PAG-3, this implies (1) the cessation of the lacustrine depositional environment of facies PAG-1 and PAG-2 and (2) a significant stratigraphic hiatus of unknown duration in the record.

### 6.1.4 Facies PAG-4: proximal mudflow and debris-flow deposits

Facies PAG-4 (29.2–4.5 mcd) encompasses poorly sorted conglomerates of light-brown color (Fig. 6f) that were deposited on top of the paleo-surface of facies PAG-3. The sediments consist of sand, gravel, and centimeter-sized pebbles in a matrix of clay and silt. Some intervals are dominated by coarse material, whereas others are marked by finer grain sizes. The matrix- to clast-supported conglomerates are structureless and lack any visible clast alignment. The overall high concentration of coarse-grained particles is reflected by NGR values as low as ∼ 50 API units (Fig. 6b). The basal depth of facies PAG-4 corresponds to the major seismic refractor and the TEM-based transition from the conductive

sediment layer to the overlying resistive layer (Fig. 3a, b), which both confirm a major lithological boundary.

Due to its poor sorting and heterogeneous character, we interpret facies PAG-4 as an amalgamated stack of proximal mudflows and debris flows along local alluvial fans, which are widespread in the catchment of the PAG clay pan (Maksaev and Marinovic, 1980). Such mudflows and debris flows are typical sedimentary processes in the Atacama Desert during heavy flood events after torrential rainfall (e.g., Mather and Hartley, 2005; Pfeiffer et al., 2021; Roldán et al., 2022). Due to the high infiltration capacity of the local soils (e.g., May et al., 2020; Pfeiffer et al., 2021), much higher torrential rainfall intensities compared to historic events are required to trigger such debris flows and mudflows (Pfeiffer et al., 2021; Wennrich et al., 2024).

#### 6.1.5 Facies PAG-5: sheetflood deposits

Facies PAG-5 is characterized by light-brownish and medium-sorted silty sand (Fig. 6e) that irregularly intercalates the conglomerates of facies PAG-4. Thicker layers of facies PAG-5 occur at 10.2–9.1, 7.0–6.5, and 5.8–5.6 mcd, where they cause distinct maxima in the NGR up to ∼ 100 API units (Fig. 6b). Thinner PAG-5 layers of only a few centimeters in thickness, which are not reflected by the NGR data, occur between 29.2 and 24.0 mcd.

The much finer grain size and better sorting of facies PAG-5 compared to PAG-4 suggest changed flow dynamics in the clay pan's catchment. The silty sand layers are massive to planar-stratified and lack an apparent grading or cross-stratification. Their stratification implies that facies PAG-5 represents a lower-energy facies derived from unconfined or poorly confined sheetfloods (May et al., 1999; Nalpas et al., 2008). The common siltstone or claystone cap of such sheetflood sandstones may have become eroded by wind or alternatively by subsequent sheetfloods or mudflow and debris flows of facies PAG-4. The upward increasing occurrence of the sheetflood deposits of facies PAG-5 and decreasing thickness might be linked to progressive starvation of distal fan lobes due to fan aggradation as a result of reduced water (and thus sediment) discharge (Bowman, 2019). Taking the ephemeral nature of the sheetflood deposits, however, we cannot exclude the possibility that the sand layers might also be associated with longer hiatuses of unknown duration.

#### 6.1.6 Facies PAG-6: pedogenic calcium sulfate

Also intercalated into the debris-flow and mudflow deposits of facies PAG-4 are two distinct sandy gravel horizons of light-brown color at approximately 3.6–3.0 and 2.3–1.2 mcd, which represent facies PAG-6 (Fig. 6a). The sandy gravel horizons show a matrix-supported fabric with a whitish cement that partly also encrusts the clasts (Fig. 6d). They are characterized by somewhat lower NGR values of ∼ 100 API units (Fig. 6b). Some clasts appear to be shattered. The lower of these cemented gravel horizons can be correlated with a calcium-sulfate duricrust identified in pilot core PAG5/6 (Ritter et al., 2019). This implies a similar pedogenic formation of facies PAG-6, as do the "floating" gravels in a matrix of calcium sulfate and dust, which are typical of calcium-sulfate paleosols (Rech et al., 2019).

Surficial calcium-sulfate crusts are widespread in the Atacama region (Ericksen, 1981; Rech et al., 2019; Voigt et al., 2020) and were also reported from other clay pans in the Coastal Cordillera (Diederich et al., 2020; Wennrich et al., 2024). The sulfate accumulation in Atacama soils is traced back to atmospheric deposition, either of primarily marine sulfate via the coastal fog, volcanic sulfate from Andean sources, or secondary atmospheric sulfate (Bao et al., 2004; Klipsch et al., 2023; Sun et al., 2018). For the PAG17 record, atmospheric and fog-induced deposition seems to be most likely, taking its considerable distance to the Andean volcanoes into account.

Pedogenesis of mature gypsic paleosols is related to overall hyperarid conditions as well as long-lasting landscape stability and non-deposition on a scale of millions of years (Ewing et al., 2006; Jordan et al., 2014; Rech et al., 2019). However, due to the restricted thickness and immature state, the gypsic paleosols in facies PAG-6 may rather be linked to shorter pedogenesis and thus shorter hiatuses in the PAG17 record. According to the age–depth model of the pilot core PAG5/6, the lower calcium-sulfate paleosol reflects a hiatus of approximately 50 kyr (Ritter et al., 2019).

#### 6.1.7 Facies PAG-7: distal alluvial sediment flow deposits

The uppermost facies, PAG-7 (1.2–0 mcd), is mainly composed of beige and powdery to compact silts and clays with only minor sand content (Fig. 6c) equal to the uppermost sediments in pilot core PAG5/6 (Ritter et al., 2019), which is much finer than the underlying facies. The more compact intervals exhibit a layered texture made up of centimeter-sized mud chips that resemble the modern clay pan surface. Observations of historic rainfall events in the Paranal clay pan implied that similar fine-grained surficial deposits represent the suspension load of distal alluvial sediment flows triggered by rare torrential rain events that occur at a decadal to centennial recurrence rate (Wennrich et al., 2024).

At around 0.5 mcd, the clays and silts are intercalated by an approximately 6 cm-thick sandy layer, which is also found in pilot core PAG5/6 (Ritter et al., 2019). Grain-size analyses of this layer in the PAG5/6 core yield a typical normal grading, which indicates deposition during a single unusually strong flood event with waning flow, whose amplitude significantly exceeded those of regular events of facies PAG-7.

### 6.2 Paranal clay pan (PAR22)

The downhole-logging results of the three holes PAR22-1A to PAR22-1C, reaching down to a maximum depth of 134 m in hole PAR22-1B, resemble similar patterns in all three parameters, with only minor deviations at the sub-meter scale (Fig. 7b, c, and d). This confirms a similar sediment succession in the center of the Paranal clay pan, at least at distances of up to 20 m between the drill holes, which is representative of the central clay pan. Thus, we decided to use the deepest hole, PAR22-1B, as the master site, which was complemented by the results of holes PAR22-1C and PAR22-1A in the middle (50–100 mcd) and upper (0–30 mcd) sections. The resultant PAR22 core composite almost exclusively consists of clastic sediments with only minor intercalations of calcium-sulfate and volcanoclastic deposits, whereas visual carbonaceous or organic components are absent. Some sediment facies in PAR22 exhibit similarities to those in PAG17, whereas other facies are unique. Based on the visual description and downhole-logging data (above 134 m), the PAR22 succession was divided into nine depositional facies (Par-1 to Par-9).

#### 6.2.1 Facies Par-1: weathered basement rock

Hole PAR22-1B penetrated approximately 3 m (174.5–171.5 mcd) into a relatively homogenous sequence of light- to dark-grey semi-consolidated rocks with intercalations of dark-greenish grey mud (Fig. 7n). The semi-consolidated rocks of facies Par-1 yield an equigranular texture of light mineral grains (quartz and feldspar) and dark mica (likely biotite). Due to the homogenous texture and the similarity to the local basement rocks outcropping on the surrounding mountains, we interpret facies Par-1 as the respective granitic to granodioritic basement of the Late Jurassic Quebrada Grande Granodiorite or Early Cretaceous Remiendos Plutonic Complex (Álvarez et al., 2016; Domagala et al., 2016). Consequently, the top of facies Par-1 at a depth of approximately 171.5 mcd (Fig. 7a) forms the surface of the local basement, which matches the TEM-based depth predictions of the sediment thickness at the drill site of $160 \pm 10$ m quite well (Blanco-Arrué et al., 2022).

The granodioritic basement rocks of facies Par-1 are heavily weathered and exhibit obvious signs of feldspar and mica alteration as well as secondary clay mineral formation along internal joints. Typical desert features, like desert varnish or hematite pigmentation, in contrast, are not observed. This clearly indicates that the upper basement rocks experienced a significant degree of chemical weathering, presumably during times of much wetter conditions than under the modern hyperarid climate.

#### 6.2.2 Facies Par-2: fluvial conglomerate

Facies Par-2 consists of an almost 110 m thick (171.5–62.0 mcd) sequence of coarse and poorly sorted clast-supported conglomerates that forms the basal sediment sequence above the basement (Fig. 7a). Clasts range from pebbles to boulders up to 1.30 m in diameter, which yield a polymictic composition (e.g., granodiorite or reddish porphyric volcanic rocks; Fig. 7m). Pockets and lenses of a yellowish-brown sand-sized matrix in between the clasts rarely occur in the lower part of the conglomerates but become more abundant towards the top. The downhole-logging data exhibit low but fluctuating MS values, whereas NGR and conductivity show higher values with a strong meter-scale variability (Fig. 7b–d) that likely mirrors the heterogeneous nature of the conglomerates. The high conductivity of the conglomerates (Fig. 7b) matches the conductive unit seen in the TEM data (Fig. 3c), although the reasons for the high conductivity are still unknown.

Due to the subrounded to well-rounded shape of the clasts and the lack of fine-clastic material in facies Par-2, we suggest that the conglomerates were deposited in a highly dynamic fluvial environment. The sediments fill a channel-like depression that is incised $\sim 80$ m into the underlying basement rocks (Fig. 3c; Blanco-Arrué et al., 2022). This channel may represent the ESE–WNW-oriented paleochannel as proposed by Herve (1987) and Scheuber and Andriessen (1990) that is assumed to have existed prior to the fault-induced drainage blocking. Based on the clast composition and shape, facies Par-2 may be linked to Early to Middle Miocene gravels of the Pampa de Mulas Fm. (Domagala et al., 2016) that were genetically correlated with the widespread Miocene Atacama gravels (Mortimer, 1973; Riquelme et al., 2007; Nalpas et al., 2008; Muñoz-Farías et al., 2023).

#### 6.2.3 Facies Par-3: fluvial sand

The fluvial conglomerate of facies Par-2 is overlain by facies Par-3 (Fig. 7a), a well-sorted and semi-consolidated red sand (62.0–52.0 mcd), which has only a few pebble-sized clasts floating in the sandy matrix (Fig. 7l). Clasts are generally more frequent in the lower part of facies Par-3 and progressively decline towards the top. The sand experiences higher but less fluctuating conductivity and MS values than the underlying conglomerate, whereas the NGR shows significantly lower values (Fig. 7b–d).

Due to the good sorting of the sand, we postulate a fluvial origin of these deposits too. The significantly finer grain size compared to the underlying conglomerates of facies Par-2 and the gradual disappearance of pebbles, however, point to a reduction in flow velocities as a result of a shift in the basin hydrology. The latter is supported by the red color of the sand that presumably results from subaerial hematite pigmentation. The hydrological change may be linked to the onset of a slow uplift of the block to the west of the modern-day clay pan along a trace of the Quebrada Grande Fault System (Blanco-Arrué et al., 2022), which may have progressively reduced the throughflow and finally led to the formation of

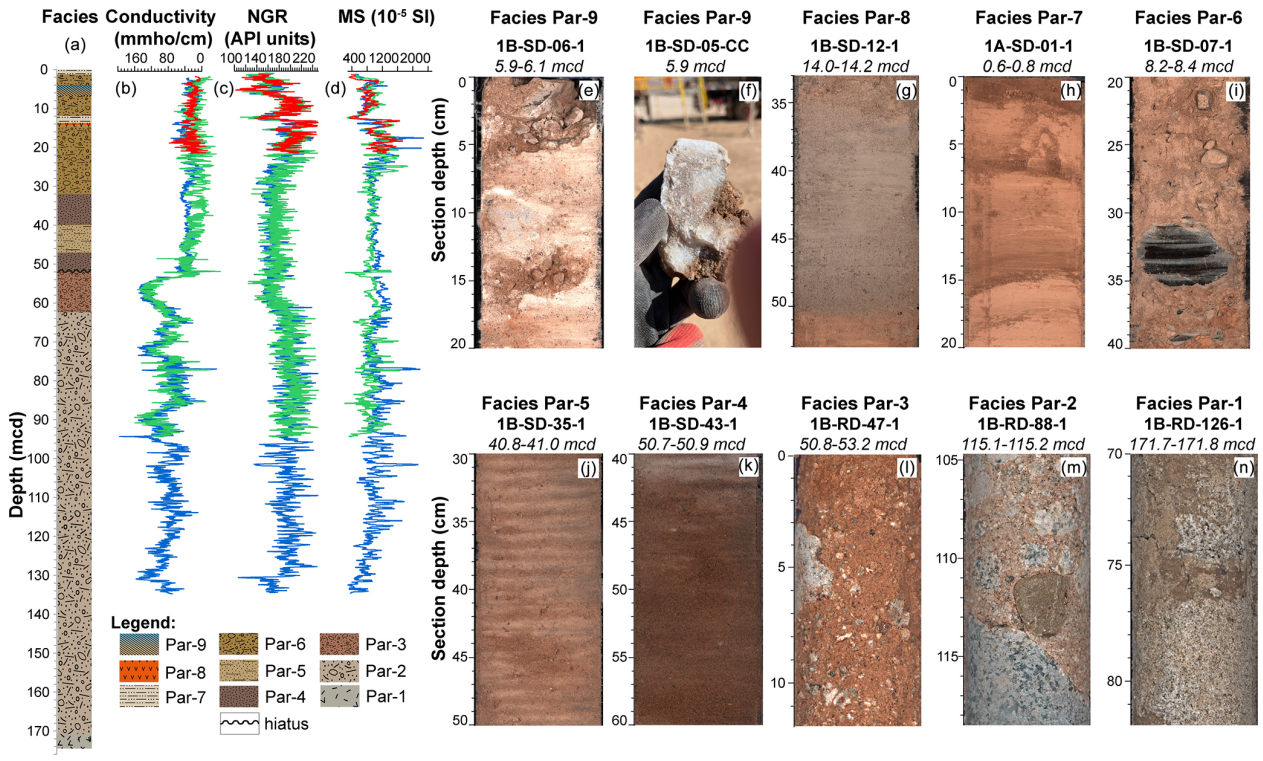


**Figure 7.** Initial results from the drilling and downhole logging at site PAR22 in the Paranal clay pan, showing the lithological facies of the core composite next to the downhole-logging-derived electrical conductivity, NGR, and MS in holes PAR22-1A (red), PAR22-1B (green), and PAR22-1C (blue). The photographs in panels **(e)**–**(n)** illustrate examples of the different sediment facies found in core PAR22.

the endorheic basin. However, climatic reasons, i.e., a significant reduction in the local precipitation, cannot be excluded at this stage as a potential reason for the reduction in fluvial transport energy.

### 6.2.4 Facies Par-4: sheetflood deposits

Facies Par-4 is characterized by a poorly to moderately sorted reddish-brown to ochre silty sand (52.0–26.0 mcd; Fig. 7a, k) with rarely intercalated pebble layers. The sand bodies have a massive to slightly planar stratification. The onset of facies Par-4 is expressed well in a major drop in the downhole-logging-derived conductivity to rather low and uniform values (Fig. 7b) corresponding to the shift from the conductive to resistive strata in the TEM data (Fig. 3c). MS and NGR values, however, stay relatively constant (Fig. 7c, d).

The silty sand of facies Par-4 shows distinct similarities to facies PAG-5 in the PAG17 record. The high silt content and the rather poor sorting contradict a purely fluvial formation of facies Par-4 but rather point to a deposition from unconfined to poorly confined sheetfloods as also reconstructed for facies PAG-5. In contrast to facies PAG-5, however, some of the sheetfloods forming facies Par-4 were obviously of higher intensity, as indicated by the intercalated pebble layers. A particularly thick and coarse-grained layer at the base of facies Par-4 in hole PAR22-1C prohibited further penetration with the sonic drill system in hole PAR22-1B. This layer most likely also caused the strong seismic refractor at ~ 60 m (Fig. 3d). Consequently, the transition of facies Par-3 to facies Par-4 marks a major shift in the hydrodynamics of the basin, from an open fluvial channel to an episodic deposition of sheetfloods in a terminal basin or clay pan.

### 6.2.5 Facies Par-5: laminated sheetflood deposits

Between 47.0 and 40.0 mcd, the silty sands of facies Par-4 are intercalated by sediments of facies Par-5 (Fig. 7a), which are marked by a distinct lamination of darker reddish sand and light-ochre silt layers of approximately 5 mm in thickness (Fig. 7j). In the Atacama Desert, such laminated sand–silt interbeddings are also associated with unconfined sheetfloods, but in contrast to facies Par-4, the deposition of the distinct silty laminae rather indicates deposition in a shallow-water environment (May et al., 1999; Nalpas et al., 2008). Thereby, the thin sand layers are believed to represent the coarser bedload from the onset of the sheetfloods, whereas the silts originate from the settling of a fine-grained suspension load during the waning phase of a flood event in a standing water body (May et al., 1999). The existence of a standing water body and the pronounced cyclicity of the local precipitation, which is implied by the rhythmic nature of the sand–silt lam-

**Figure 8.** Boulder field to the east of the Paranal clay pan as a remnant of a debris flow from local alluvial fans.

ination, strongly differs from the modern conditions in the Paranal clay pan (Wennrich et al., 2024).

#### 6.2.6 Facies Par-6: proximal mudflow and debris-flow deposits

At ~ 26.0 mcd the distal alluvial deposits of facies Par-4 are progressively replaced by more coarse-grained and poorly sorted sand and gravel of facies Par-6 (Fig. 7a), which contain abundant pebble layers (Fig. 7i). The coarse-grained sediment components have probably led to elevated MS values, which reach their maxima in the core, although with strong fluctuations (Fig. 7d). Simultaneously, the NGR values show a broad maximum intersected by a few distinct minima (Fig. 7c).

Based on the similarities in the lithological properties of facies Par-6 to facies PAG-4 in core PAG17, we also trace this facies back to a series of amalgamated debris flows and mudflows from adjacent alluvial fans, which occur to the north and south of the clay pan or alternatively as overland flows. This interpretation is supported by boulder fields at the edges of the modern Paranal clay pan (Fig. 8), which presumably represent the coarse remnants of such high-energy debris flows, with the finer fractions progressively eroded by wind and/or subsequent floods.

#### 6.2.7 Facies Par-7: distal alluvial sediment flow deposits

In the proximal alluvial deposits of facies Par-6, two intervals are incised (approximately 15.5–12.1 mcd; approximately 1.0 mcd – top; Fig. 7a), which differ from Par-6 by their much finer clastic material, i.e., by powdery clayey silt with only traces of sand (Fig. 7h). The finer grain size of this facies Par-7 corresponds to lower NGR and MS values (Fig. 7c, d).

Facies Par-7 is lithologically very similar to facies PAG-7 in core PAG17, indicating a similar formation by alluvial sediment flows. The upper one of the two facies Par-7 intervals was also recovered in pilot core PAR-1, where it was dated to the Holocene and attributed to distal overland flows or mudflows triggered by moderate rainfall events > 20 mm (Wennrich et al., 2024). Additionally, six to seven darker coarse silt layers occur in both core PAR-1 and the upper horizon of facies Par-7 in drill core PAR22 (Fig. 7h). These dark layers in core PAR-1 were attributed to "Millennial-scale rain events", whose intensities significantly exceeded any historic rainfall (Wennrich et al., 2024). However, due to the limited age control on the record, the question is as yet unsolved as to when exactly these events occurred and whether they are synchronous with higher-amplitude flood events in the Holocene succession of the Herradura clay pan near Yungay (Arens et al., 2024).

#### 6.2.8 Facies Par-8: volcanic ash deposit

At a depth of 14.2–14.0 mcd, an approximately 15 cm greyish unit (Fig. 7g) is intercalated into the fine-grained beige clay pan sediments of facies Par-7 (Fig. 7a). This facies Par-8 is a volcanic ash deposit, which is confirmed by microscopic investigations that yielded abundant volcanic glass shards. The tephra layer exhibits a clear fining-upward trend from fine sand at the base to silt towards the top. Due to the comparably fine grain size of the tephra and the absence of an erosive base, a rather distal volcanic eruption, presumably in the Altiplano–Puna volcanic complex (APVC; de Silva, 1989) or the southern Central Andes Volcanic Zone (SCVZ; Stern, 2004), can be assumed to be the source of the tephra. A definitive correlation with a specific volcanic center or even a certain eruption, however, requires a comprehensive study of the glass major and trace element geochemistry. Other macroscopically visible tephra layers are lacking in both the PAG17 and PAR22 records. This is surprising given the large number of tephra layers outcropping in the Atacama Desert in general and in the vicinities of the investigated clay pans in particular (e.g., Placzek et al., 2009; Breitkreuz et al., 2014; Ritter et al., 2022).

#### 6.2.9 Facies Par-9: pedogenic calcium sulfate

Facies Par-9 is incised in facies Par-7 at a depth of approximately 6.0–4.0 mcd (Fig. 7a). It is composed of coarse-grained sand and gravel-rich strata that are cemented by a fine-grained whitish matrix (Fig. 7e). This horizon is also visible in the downhole-logging data as a minimum in the NGR data (Fig. 7c).

Facies Par-9 has a striking similarity to facies PAG-6 in core PAG17, suggesting a common formation as calcium-sulfate paleosols. As mentioned before, due to the slow accumulation of atmospheric sulfates, the pedogenesis of calcium-sulfate-rich soils in the Atacama requires long-term

stable arid conditions (Ritter et al., 2022) and is often linked to phases of low deposition or non-deposition (Jordan et al., 2014; Rech et al., 2019). Thus, facies Par-9 likely represents a certain hiatus in the PAR22 record, presumably due to either climatic or tectonic-induced alluvial-fan starvation. In contrast to facies PAG-6, however, at approximately 5.9 mcd depth facies Par-9 also contains a distinct cobble layer made of well-crystallized gypsum (Fig. 7f), which was unfortunately only recovered in the core catcher of one of the PAR22 runs. The nature of such crystalline gypsum excludes a pedogenic formation and rather points to precipitation from sulfate-saturated waters. This side-by-side occurrence of pedogenic and lacustrine or groundwater gypsum in facies Par-9, which might involve phases of recrystallization, is not yet understood and needs further investigation.

## 7 Paleo-environmental and climatic implications

The various sedimentary facies recovered in the PAG17 and PAR22 drill cores illustrate specific depositional environments in the two basins that are controlled by the paleoclimate conditions and basin-specific characteristics as well as their tectonic evolution. Despite being only 250 km apart, both drill cores yield some major differences in their sedimentary facies, especially in the lower part of the cores. In the upper part, in contrast, both cores have some similar sediment facies, although with discrepancies in their specific successions.

The basal sediments in the PAR22 core above the basement rocks consist of a thick sequence of fluvial conglomerates and sands that represent a deposition in an open fluvial system prior to the tectonic blocking. Such a fluvial system implies a more constant water throughflow and thus significantly wetter conditions than today, presumably prior to the postulated intensification of hyperaridity in the Atacama Desert since the Miocene (e.g., Amundson et al., 2012; Dunai et al., 2005; Evenstar et al., 2009; Rech et al., 2019). These pre-blocking sediments were, however, not recovered from the PAG clay pan.

Due to the tectonic blocking, both the PAG and Paranal systems became closed terminal basins. These events are displayed through different lithological facies and must not be contemporaneous. In the PAG basin, the initial tectonic blocking formed a large permanent lake likely fed by surface water and local groundwater flows. The lack of erosional features in the fine-grained facies PAG-1 suggests that the local precipitation in the catchment balanced and/or exceeded evaporation from the lake surface over a longer period, which requires significantly more precipitation compared to today. Recurring calcium-sulfate intercalations of facies PAG-2, however, imply cyclic calcium-sulfate (likely gypsum) precipitation due to an enhanced evaporation–precipitation. In the Paranal basin, in contrast, the post-blocking deposits consist of sheetflood deposits of facies Par-4 and Par-5 that contradict persistent lacustrine conditions and rather point to an episodic alluvial deposition in a temporary shallow-water environment. As the timing of the ponding of both clay pans is still poorly constrained, the differences in the PAG and Paranal post-blocking successions might be due to different precipitation regimes at both sites after the tectonic blocking. However, differences in the basin characteristics may have been influential, like the closer proximity of the Paranal site to the local alluvial fans or the availability of local groundwater.

The thick proximal mudflow and debris-flow deposits of facies PAG-4 and Par-6 illustrate that at some point the deposition in both basins was fully controlled by the strong although episodic activity of the local alluvial systems without significant groundwater influence. High infiltration rates of the local hillslope soils in both clay pan catchments, however, require much more intense torrential rainfall rates compared to today to generate such mudflows and debris flows (Wennrich et al., 2024) and enable the propagation of local alluvial fans towards the drill sites. Intercalated paleosols of facies Par-9 and PAG-6 in the upper parts of the mudflow and debris-flow deposits in both cores suggest that depositional episodes were progressively interrupted by longer-lasting phases of non-deposition and soil formation.

Distal alluvial sediment flow deposits of facies Par-7 and PAG-7 on top of the sediment sequences of both clay pans illustrate another change in the sedimentary processes in both catchments to dominating distal overland flows or mudflows. This lower-energy deposition implies a decreasing proximity of the alluvial-fan drainages, presumably caused by a progressive climatic and/or tectonic-induced alluvial-fan starvation.

Overall, the facies successions of both cores indicate a similar evolution from wetter conditions with more persistent rainfall to more episodic precipitation patterns. In the following, the increasing occurrence of paleosols and the signs of progressive fan starvation towards the top suggest aridification trends that are noticeable at both sites. Differences in the facies distributions between the two records, however, might be due to differences in the site sensitivities, e.g., different rain-rate thresholds for the initiation of surface runoff. Alternatively, these differences can also point to larger discrepancies in the core ages or heterogeneities in the precipitation histories of both clay pan areas.

## 8 Conclusions and outlook

Comprehensive studies of two clay pans in the Coastal Cordillera of northern Chile, i.e., the PAG and Paranal clay pans, applying multi-method site surveys, deep drillings, and downhole logging, allow some fundamental conclusions concerning their potential as archives of the Neogene–Quaternary precipitation history of the Atacama Desert.

Multidisciplinary analyses of the up to 6.2 m long pilot cores reveal highly variable near-surface sediments in the two clay pans based on their sedimentological, geochemical, mineralogical, and biological compositions. These different characteristics reflect different depositional settings in response to hydroclimatic fluctuations in the catchments of the clay pans. The chronology of the pilot cores, developed through a combination of different dating techniques such as radiocarbon and luminescence dating as well as magnetostratigraphy, implies sediment formation since MIS 3 and MIS 7 for the Paranal and PAG sites, respectively, although partly discontinuous.

From the geophysical site surveys it becomes evident that the clay pans host sediment records that are more than 100 m thick. Extrapolations of the sedimentation rates of the pilot cores suggest that the sediment records in the clay pans cover several million years. The basement morphology of the PAG clay pan exhibits a simple bowl-shaped geometry, whereas an incised channel of up to 80 m is suggested underneath the Paranal clay pan. In both clay pans, the TEM data imply a three-layer structure, with the resistive basement overlain by a low-resistivity basal sediment unit and an upper sediment unit with significantly higher resistivities. According to the seismic velocity model, which reaches up to 70 m into the sediments, the upper sediments show a few distinct seismic refractors as evidence of lithological boundaries, which exhibit only little horizontal variability.

The lithological description of the drill cores and the downhole-logging data clearly show that the lower resistivity of the lower sediment units does not reflect the same facies, but two very different sediment facies. In the case of the PAG clay pan, the low-resistivity unit is composed of an alternation of fine-grained clastic and evaporitic playa lake deposits, whereas coarse-grained fluvial conglomerates and sandstones built the lower sediment unit in the Paranal clay pan. In contrast, the overlying sediments in both clay pans show numerous similar facies, which reflect proximal mudflows and debris flows, sheetfloods, distal alluvial sediment flows, and pedogenic calcium sulfates but differ in their individual facies successions. A macroscopically visible volcanic ash layer is found in the Paranal clay pan but is absent in the core from the PAG clay pan. Both cores are similar in that they contain sediments whose deposition, e.g., in a permanent lake and a fluvial setting, reflects much more humid conditions than those reconstructed from the pilot cores for the last glacial–interglacial cycles. The differences in the facies distribution between the two records, however, indicate that they differ in age, but the differences probably also reflect different precipitation histories despite their relatively close proximity.

Drill cores PAG17 and PAR22 are currently being investigated in detail for their sedimentology, geochemistry, mineralogy, and paleoecology. One of the most challenging aspects is to achieve robust chronologies. Radiocarbon and luminescence datings, which are important methods for the chronology in the uppermost sediments, might already exceed their maximal datable time ranges of $\leq 55$ ka (Hogg et al., 2020; Wagner, 1998) or $< 1$ Ma (Ankjærgaard et al., 2013; Zander and Hilgers, 2013) within the first core meters. Therefore, further methods for determining age constraints shall be applied, including tephrochronology, magnetostratigraphy, and U-series dating of evaporites. Furthermore, cosmogenic nuclide burial dating of quartz as well as meteoric $^{10}$Be dating might provide additional chronological tie points with theoretical limits as far back as the Middle Miocene (Balco and Shuster, 2009; Ma et al., 2018; Lebatard et al., 2010). The results will provide unprecedented information on the long-term precipitation history in the hyperarid core of the Atacama Desert, which shall be discussed in the light of global and regional tectonic, oceanographic, and atmospheric changes.

**Data availability.** Downhole-logging data of the PAG17 and PAR22 drillings as well as CNE dating results of the Paranal paleodrainage are available from the CRC1211 database (https://www.crc1211db.uni-koeln.de/search/view.php?dataID=1031, Wennrich et al., 2025).

**Author contributions.** The initial project idea was developed by VW, TD, and MM. The financial support for the drilling operations was acquired by VW and MM. VW, JDL, BNBA, CB, SB, LN, and PY planned and performed the geophysical surveys. VW, JDL, TD, and BR performed the pilot coring. VW, JDL, ECS, EG, AH, DAL, JM, and AM participated in the logistics and fieldwork of the PAG17 drilling. VW, ECS, JF, DAL, JM, RP, JCRC, and BVM participated in the Paranal deep drilling. NL analyzed the tephra sample in the PAR22 core, and BR conducted the CNE dating of the quartz pebbles. VW, JDL, BNBA, SS, and MM prepared the original manuscript with contributions from all of the co-authors. Visualization of the data and maps was done by VW, JDL, BNBA, and BR.

**Competing interests.** The contact author has declared that none of the authors has any competing interests.

**Disclaimer.** Publisher's note: Copernicus Publications remains neutral with regard to jurisdictional claims made in the text, published maps, institutional affiliations, or any other geographical representation in this paper. While Copernicus Publications makes every effort to include appropriate place names, the final responsibility lies with the authors.

**Acknowledgements.** First of all, we want to thank our colleagues at the Universidad Católica del Norte (UCN) Antofagasta for the endless logistical support during the field campaigns. The PAR22 drilling was conducted on the premises of the European Southern Observatory (ESO) and was done with the express written permis-

sion of ESO and in accordance with Chilean national and local regulations as well as ESO safety rules. We are also grateful to the Servicio Nacional de Geología y Minería (SERNAGEOMIN), who kindly gave us permission for the deep drillings in 2017 and 2022. Thomas Wonik and Thomas Grelle at the Leibniz Institute for Applied Geophysics (LIAG) are thanked for making the NGR downhole-logging equipment for the PAR17 drilling campaign available. The Geophysical Instrument Pool Potsdam and Klaus Bataille (Universidad de Concepción) generously provided the seismic field equipment and Daniel Díaz (University of Chile) the ABEM Walk TEM system. Special thanks go to Nicole Mantke, Dorothea Klinghardt (deceased), and various student assistants for their support during the analytical work at the University of Cologne, as well as Wiebke Mörbe and Peggy Gödickmeier for the successful collaboration and support during the geophysical field campaigns.

**Financial support.** This research has been supported by the Deutsche Forschungsgemeinschaft (DFG) as part of Collaborative Research Centre (CRC) 1211 "Earth – Evolution at the Dry Limit", sub-project A02 (grant nos. SFB 1211/2 2016 and SFB 1211/2 2020).

**Review statement.** This paper was edited by Hendrik Vogel and reviewed by Torsten Haberzettl and two anonymous referees.

## References

Allmendinger, R. W. and González, G.: Invited review paper: Neogene to Quaternary tectonics of the coastal Cordillera, northern Chile, Tectonophysics, 495, 93–110, https://doi.org/10.1016/j.tecto.2009.04.019, 2010.

Álvarez, J., Jorquera, R., Mirales, C., Padel, M., and Martínez, P.: Cartas Punta Posallaves y Sierra Vicuña Mackenna: Región de Antofagasta, Serie Geología Básica, Servicio Nacional de Geología y Minería, Subdirección Nacional de Geología, Santiago, 183–184, 147 pp., ISSN 0717-7283, 2016.

Amundson, R., Dietrich, W., Bellugi, D., Ewing, S., Nishiizumi, K., Chong, G., Owen, J., Finkel, R., Heimsath, A., Stewart, B., and Caffee, M.: Geomorphologic evidence for the late Pliocene onset of hyperaridity in the Atacama Desert, Geol. Soc. Am. Bull., 124, 1048–1070, https://doi.org/10.1130/b30445.1, 2012.

Ankjærgaard, C., Jain, M., and Wallinga, J.: Towards dating Quaternary sediments using the quartz Violet Stimulated Luminescence (VSL) signal, Quat. Geochronol., 18, 99–109, https://doi.org/10.1016/j.quageo.2013.06.001, 2013.

Arens, F. L., Feige, J., Airo, A., Sager, C., Hecht, L., Horstmann, L., Kaufmann, F. E. D., Lachner, J., Neumann, T., Nowaczyk, N., Schiperski, F., Steier, P., Stoll, A., Struck, U., Valenzuela, B., von Blanckenburg, F., Wittmann, H., Wacker, L., Wagner, D., Zamorano, P., and Schulze-Makuch, D.: Climate variability in a 3.8 Ma old sedimentary record from the hyperarid Atacama Desert, Global Planet. Change, 242, 104576, https://doi.org/10.1016/j.gloplacha.2024.104576, 2024.

Baker, P. A., Seltzer, G. O., Fritz, S. C., Dunbar, R. B., Grove, M. J., Tapia, P. M., Cross, S. L., Rowe, H. D., and Broda, J. P.: The History of South American Tropical Precipitation for the Past 25 000 Years, Science, 291, 640–643, https://doi.org/10.1126/science.291.5504.640, 2001.

Balco, G. and Shuster, D. L.: 26Al–10Be–21Ne burial dating, Earth Planet. Sc. Lett., 286, 570–575, https://doi.org/10.1016/j.epsl.2009.07.025, 2009.

Bao, H., Jenkins, K. A., Khachaturyan, M., and Díaz, G. C.: Different sulfate sources and their post-depositional migration in Atacama soils, Earth Planet. Sc. Lett., 224, 577–587, https://doi.org/10.1016/j.epsl.2004.05.006, 2004.

Barrow, J. C.: The Resonant Sonic Drilling Method: An Innovative Technology for Environmental Restoration Programs, Groundwater Monitoring & Remediation, 14, 153–160, https://doi.org/10.1111/j.1745-6592.1994.tb00110.x, 1994.

Blanco Arrué, B.: Multidimensional inversion of transient electromagnetic data for the exploration of clay pans in the Atacama Desert, Chile, PhD thesis, University of Cologne, Germany, 125 pp., 2024.

Blanco-Arrué, B., Yogeshwar, P., Tezkan, B., Mörbe, W., Díaz, D., Farah, B., Buske, S., Ninneman, L., Domagala, J. P., Diederich-Leicher, J. L., Gebhardt, A. C., and Wennrich, V.: Exploration of sedimentary deposits in the Atacama Desert, Chile, using integrated geophysical techniques, J. S. Am. Earth Sci., 115, 103746, https://doi.org/10.1016/j.jsames.2022.103746, 2022.

Bobst, A. L., Lowenstein, T. K., Jordan, T. E., Godfrey, L. V., Ku, T.-L., and Luo, S.: A 106ka paleoclimate record from drill core of the Salar de Atacama, northern Chile, Palaeogeogr. Palaeocl., 173, 21–42, https://doi.org/10.1016/S0031-0182(01)00308-X, 2001.

Bowman, D.: Aggradation, in: Principles of Alluvial Fan Morphology, Springer Netherlands, Dordrecht, 57–60, https://doi.org/10.1007/978-94-024-1558-2_7, 2019.

Breitkreuz, C., de Silva, S. L., Wilke, H. G., Pfänder, J. A., and Renno, A. D.: Neogene to Quaternary ash deposits in the Coastal Cordillera in northern Chile: Distal ashes from supereruptions in the Central Andes, J. Volcanol. Geoth. Res., 269, 68–82, https://doi.org/10.1016/j.jvolgeores.2013.11.001, 2014.

Coira, B., Davidson, J., Mpodozis, C., and Ramos, V.: Tectonic and magmatic evolution of the Andes of northern Argentina and Chile, Earth-Sci. Rev., 18, 303–332, https://doi.org/10.1016/0012-8252(82)90042-3, 1982.

Criado-Reyes, J., Otálora, F., Canals, À., Verdugo-Escamilla, C., and García-Ruiz, J.-M.: Mechanisms shaping the gypsum stromatolite-like structures in the Salar de Llamara (Atacama Desert, Chile), Sci. Rep., 13, 678, https://doi.org/10.1038/s41598-023-27666-5, 2023.

de Silva, S. L.: Altiplano-Puna volcanic complex of the central Andes, Geology, 17, 1102–1106, https://doi.org/10.1130/0091-7613(1989)017<1102:Apvcot>2.3.Co;2, 1989.

Díaz, F. P., Latorre, C., Maldonado, A., Quade, J., and Betancourt, J. L.: Rodent middens reveal episodic, long-distance plant colonizations across the hyperarid Atacama Desert over the last 34 000 years, J. Biogeogr., 39, 510–525, https://doi.org/10.1111/j.1365-2699.2011.02617.x, 2012.

Diederich, J. L., Wennrich, V., Bao, R., Büttner, C., Bolten, A., Brill, D., Buske, S., Campos, E., Fernández-Galego, E., Gödickmeier, P., Ninnemann, L., Reyers, M., Ritter, B., Ritterbach, L., Rolf, C., Scheidt, S., Dunai, T. J., and Melles, M.: A 68 ka precipitation record from the hyperarid core of the Atacama

Desert in northern Chile, Global Planet. Change, 184, 103054, https://doi.org/10.1016/j.gloplacha.2019.103054, 2020.

Domagala, J., Escribano, J., De La Cruz, R., Saldias, J., and Joquera, R.: Cartas Blanco Encalada y Pampa Remiendos, Region de Antofagasta, Serie Geología Básica, Servicio Nacional de Geología y Minería, Subdirección Nacional de Geología, Santiago, 187–188, 97 pp., ISSN 0717-7283, 2016.

Dunai, T. J., González López, G. A., and Juez-Larré, J.: Oligocene–Miocene age of aridity in the Atacama Desert revealed by exposure dating of erosion-sensitive landforms, Geology, 33, 321–324, https://doi.org/10.1130/g21184.1, 2005.

Dunai, T. J., Melles, M., Quandt, D., Knief, C., and Amelung, W.: Whitepaper: Earth – Evolution at the dry limit, Global Planet. Change, 193, 103275, https://doi.org/10.1016/j.gloplacha.2020.103275, 2020.

Elgueta, M. and Barría, C.: Registro en Altura de *Enodisoma curtipennis* Cigliano, 1989 (Orthoptera: Tristiridae), en la Zona Costera Sur de la Región de Antofagasta, Boletín Museo Nacional de Historia Natural, 57, 133–138, https://doi.org/10.54830/bmnhn.v57.2008.252, 2008.

Ericksen, G. E.: Geology and origin of the Chilean nitrate deposits, USGS Professional paper 1188, 37 pp., https://doi.org/10.3133/pp1188, 1981.

Evenstar, L. A., Hartley, A. J., Stuart, F. M., Mather, A. E., Rice, C. M., and Chong, G.: Multiphase development of the Atacama Planation Surface recorded by cosmogenic 3He exposure ages: Implications for uplift and Cenozoic climate change in western South America, Geology, 37, 27–30, https://doi.org/10.1130/g25437a.1, 2009.

Evenstar, L. A., Mather, A. E., Hartley, A. J., Stuart, F. M., Sparks, R. S. J., and Cooper, F. J.: Geomorphology on geologic timescales: Evolution of the late Cenozoic Pacific paleosurface in Northern Chile and Southern Peru, Earth-Sci. Rev., 171, 1–27, https://doi.org/10.1016/j.earscirev.2017.04.004, 2017.

Ewing, S. A., Sutter, B., Owen, J., Nishiizumi, K., Sharp, W., Cliff, S. S., Perry, K., Dietrich, W., McKay, C. P., and Amundson, R.: A threshold in soil formation at Earth's arid–hyperarid transition, Geochim. Cosmochim. Ac., 70, 5293–5322, https://doi.org/10.1016/j.gca.2006.08.020, 2006.

Fritz, S. C., Baker, P. A., Lowenstein, T. K., Seltzer, G. O., Rigsby, C. A., Dwyer, G. S., Tapia, P. M., Arnold, K. K., Ku, T.-L., and Luo, S.: Hydrologic variation during the last 170 000 years in the southern hemisphere tropics of South America, Quaternary Res., 61, 95–104, https://doi.org/10.1016/j.yqres.2003.08.007, 2004.

Garreaud, R. D., Vuille, M., Compagnucci, R., and Marengo, J.: Present-day South American climate, Palaeogeogr. Palaeocl., 281, 180–195, https://doi.org/10.1016/j.palaeo.2007.10.032, 2009.

Garreaud, R. D., Molina, A., and Farias, M.: Andean uplift, ocean cooling and Atacama hyperaridity: A climate modeling perspective, Earth Planet. Sc. Lett., 292, 39–50, https://doi.org/10.1016/j.epsl.2010.01.017, 2010.

González, G., Pasten-Araya, F., Victor, P., González, Y., Valenzuela, J., and Shrivastava, M.: The role of interplate locking on the seismic reactivation of upper plate faults on the subduction margin of northern Chile, Sci. Rep., 11, 21444, https://doi.org/10.1038/s41598-021-00875-6, 2021.

Harrington, H. J.: Geology of Parts of Antofagasta and Atacama Provinces, Northern Chile1, AAPG Bull., 45, 169–197, https://doi.org/10.1306/0bda6332-16bd-11d7-8645000102c1865d, 1961.

Hartley, A. J. and Chong, G.: Late Pliocene age for the Atacama Desert: Implications for the desertification of western South America, Geology, 30, 43–46, https://doi.org/10.1130/0091-7613(2002)030<0043:Lpafta>2.0.Co;2, 2002.

Hartley, A. J., Chong, G., Houston, J., and Mather, A. E.: 150 million years of climatic stability: evidence from the Atacama Desert, northern Chile, J. Geol. Soc., 162, 421–424, https://doi.org/10.1144/0016-764904-071, 2005.

Herve, M.: Movimiento normal de la falla Paposo, Zona de Falla Atacama, en el Mioceno, Chile, Andean Geol., 31, 31–36, 1987.

Hogg, A. G., Heaton, T. J., Hua, Q., Palmer, J. G., Turney, C. S. M., Southon, J., Bayliss, A., Blackwell, P. G., Boswijk, G., Bronk Ramsey, C., Pearson, C., Petchey, F., Reimer, P., Reimer, R., and Wacker, L.: SHCal20 Southern Hemisphere Calibration, 0–55 000 Years cal BP, Radiocarbon, 62, 759–778, https://doi.org/10.1017/rdc.2020.59, 2020.

Houston, J.: Variability of precipitation in the Atacama Desert: its causes and hydrological impact, Int. J. Climatol., 26, 2181–2198, https://doi.org/10.1002/joc.1359, 2006.

Houston, J. and Hartley, A. J.: The central Andean west-slope rainshadow and its potential contribution to the origin of hyperaridity in the Atacama Desert, Int. J. Climatol., 23, 1453–1464, 2003.

Jordan, T. E., Kirk-Lawlor, N. E., Blanco, N. P., Rech, J. A., and Cosentino, N. J.: Landscape modification in response to repeated onset of hyperarid paleoclimate states since 14 Ma, Atacama Desert, Chile, GSA Bulletin, 126, 1016–1046, https://doi.org/10.1130/b30978.1, 2014.

Klipsch, S., Herwartz, D., Voigt, C., Münker, C., Chong, G., Böttcher, M. E., and Staubwasser, M.: Sulfate sources, biologic cycling, and mobility in Atacama Desert soils revealed by isotope signatures, Global Planet. Change, 230, 104290, https://doi.org/10.1016/j.gloplacha.2023.104290, 2023.

Labbé, N., García, M., Simicic, Y., Contreras-Reyes, E., Charrier, R., De Pascale, G., and Arriagada, C.: Sediment fill geometry and structural control of the Pampa del Tamarugal basin, northern Chile, GSA Bulletin, 131, 155–174, https://doi.org/10.1130/b31722.1, 2018.

Latorre, C., Betancourt, J. L., Rylander, K. A., and Quade, J.: Vegetation invasions into absolute desert: A 45 000 yr rodent midden record from the Calama–Salar de Atacama basins, northern Chile (lat 22–24 S), Geol. Soc. Am. Bull., 114, 349–366, 2002.

Lebatard, A.-E., Bourlès, D. L., Braucher, R., Arnold, M., Duringer, P., Jolivet, M., Moussa, A., Deschamps, P., Roquin, C., Carcaillet, J., Schuster, M., Lihoreau, F., Likius, A., Mackaye, H. T., Vignaud, P., and Brunet, M.: Application of the authigenic 10Be/9Be dating method to continental sediments: Reconstruction of the Mio-Pleistocene sedimentary sequence in the early hominid fossiliferous areas of the northern Chad Basin, Earth Planet. Sc. Lett., 297, 57–70, https://doi.org/10.1016/j.epsl.2010.06.003, 2010.

Ma, Y., Wang, W., Zheng, D., Zhang, H., Pang, J., Wu, Y., Stuart, F. M., and Xu, S.: Mid-Miocene cosmogenic upper limit for $^{10}Be$ / $^{21}Ne$ burial age, Quat. Geochronol., 48, 72–79, https://doi.org/10.1016/j.quageo.2018.08.004, 2018.

Maksaev, V. and Marinovic, N.: Geología de los cuadrángulos Cerro de La Mica, Quillagua, Cerro Posada y Oficina Prosperidad, Región de Antofagasta, 1980.

Maldonado, A., Betancourt, J. L., Latorre, C., and Villagran, C.: Pollen analyses from a 50 000-yr rodent midden series in the southern Atacama Desert (25°30′ S), J. Quaternary Sci., 20, 493–507, https://doi.org/10.1002/jqs.936, 2005.

Mather, A. E. and Hartley, A.: Flow events on a hyper-arid alluvial fan: Quebrada Tambores, Salar de Atacama, northern Chile, Geol. Soc. Spec. Publ., 251, 9–24, https://doi.org/10.1144/GSL.SP.2005.251.01.02, 2005.

May, G., Hartley, A. J., Stuart, F. M., and Chong, G.: Tectonic signatures in arid continental basins: an example from the Upper Miocene–Pleistocene, Calama Basin, Andean forearc, northern Chile, Palaeogeogr. Palaeocl., 151, 55–77, https://doi.org/10.1016/S0031-0182(99)00016-4, 1999.

May, S. M., Meine, L., Hoffmeister, D., Brill, D., Medialdea, A., Wennrich, V., Gröbner, M., Schulte, P., Steininger, F., Deprez, M., de Kock, T., and Bubenzer, O.: Origin and timing of past hillslope activity in the hyper-arid core of the Atacama Desert – The formation of fine sediment lobes along the Chuculay Fault System, Northern Chile, Global Planet. Change, 184, 103057, https://doi.org/10.1016/j.gloplacha.2019.103057, 2020.

Mortimer, C.: The Cenozoic history of the southern Atacama Desert, Chile, J. Geol. Soc., 129, 505–526, https://doi.org/10.1144/gsjgs.129.5.0505, 1973.

Muñoz-Farías, S., Ritter, B., Dunai, T. J., Morales-Leal, J., Campos, E., Spikings, R., and Riquelme, R.: Geomorphological significance of the Atacama Pediplain as a marker for the climatic and tectonic evolution of the Andean forearc, between 26° to 28° S, Geomorphology, 420, 108504, https://doi.org/10.1016/j.geomorph.2022.108504, 2023.

Nalpas, T., Dabard, M. P., Ruffet, G., Vernon, A., Mpodozis, C., Loi, A., and Hérail, G.: Sedimentation and preservation of the Miocene Atacama Gravels in the Pedernales–Chañaral Area, Northern Chile: Climatic or tectonic control?, Tectonophysics, 459, 161–173, https://doi.org/10.1016/j.tecto.2007.10.013, 2008.

Nunnery, J. A., Fritz, S. C., Baker, P. A., and Salenbien, W.: Lake-level variability in Salar de Coipasa, Bolivia during the past ∼40 000 yr, Quaternary Res., 91, 881–891, https://doi.org/10.1017/qua.2018.108, 2019.

Owen, J. J., Dietrich, W. E., Nishiizumi, K., Chong, G., and Amundson, R.: Zebra stripes in the Atacama Desert: Fossil evidence of overland flow, Geomorphology, 182, 157–172, https://doi.org/10.1016/j.geomorph.2012.11.006, 2013.

Pfeiffer, M., Latorre, C., Santoro, C. M., Gayo, E. M., Rojas, R., Carrevedo, M. L., McRostie, V. B., Finstad, K. M., Heimsath, A., Jungers, M. C., De Pol-Holz, R., and Amundson, R.: Chronology, stratigraphy and hydrological modelling of extensive wetlands and paleolakes in the hyperarid core of the Atacama Desert during the late quaternary, Quat. Sci. Rev., 197, 224–245, https://doi.org/10.1016/j.quascirev.2018.08.001, 2018.

Pfeiffer, M., Morgan, A., Heimsath, A., Jordan, T., Howard, A., and Amundson, R.: Century scale rainfall in the absolute Atacama Desert: Landscape response and implications for past and future rainfall, Quat. Sci. Rev., 254, 106797, https://doi.org/10.1016/j.quascirev.2021.106797, 2021.

Pizarro, H., Rousse, S., Riquelme, R., Veloso, E., Campos, E., González, R., Bissig, T., Carretier, S., Fernández-Mort, A., and Muñoz, S.: The origin of the magnetic record in Eocene-Miocene coarse-grained sediments deposited in hyper-arid/arid conditions: Examples from the Atacama Desert, Palaeogeogr. Palaeocl., 516, 322–335, https://doi.org/10.1016/j.palaeo.2018.12.009, 2019.

Placzek, C., Quade, J., Rech, J. A., Patchett, P. J., and Pérez de Arce, C.: Geochemistry, chronology and stratigraphy of Neogene tuffs of the Central Andean region, Quat. Geochronol., 4, 22–36, https://doi.org/10.1016/j.quageo.2008.06.002, 2009.

Quade, J., Rech, J. A., Betancourt, J. L., Latorre, C., Quade, B., Rylander, K. A., and Fisher, T.: Paleowetlands and regional climate change in the central Atacama Desert, northern chile, Quaternary Res., 69, 343–360, https://doi.org/10.1016/j.yqres.2008.01.003, 2008.

Rech, J. A., Currie, B. S., Shullenberger, E. D., Dunagan, S. P., Jordan, T. E., Blanco, N., Tomlinson, A. J., Rowe, H. D., and Houston, J.: Evidence for the development of the Andean rain shadow from a Neogene isotopic record in the Atacama Desert, Chile, Earth Planet. Sc. Lett., 292, 371–382, https://doi.org/10.1016/j.epsl.2010.02.004, 2010.

Rech, J. A., Currie, B. S., Jordan, T. E., Riquelme, R., Lehmann, S. B., Kirk-Lawlor, N. E., Li, S., and Gooley, J. T.: Massive middle Miocene gypsic paleosols in the Atacama Desert and the formation of the Central Andean rain-shadow, Earth Planet. Sc. Lett., 506, 184–194, https://doi.org/10.1016/j.epsl.2018.10.040, 2019.

Reyers, M., Boehm, C., Knarr, L., Shao, Y., and Crewell, S.: Synoptic-to-Regional-Scale Analysis of Rainfall in the Atacama Desert (18°–26° S) Using a Long-Term Simulation with WRF, Mon. Weather Rev., 149, 91–112, https://doi.org/10.1175/mwr-d-20-0038.1, 2021.

Riquelme, R., Hérail, G., Martinod, J., Charrier, R., and Darrozes, J.: Late Cenozoic geomorphologic signal of Andean forearc deformation and tilting associated with the uplift and climate changes of the Southern Atacama Desert (26° S–28° S), Geomorphology, 86, 283–306, https://doi.org/10.1016/j.geomorph.2006.09.004, 2007.

Ritter, B., Stuart, F. M., Binnie, S. A., Gerdes, A., Wennrich, V., and Dunai, T. J.: Neogene fluvial landscape evolution in the hyperarid core of the Atacama Desert, Sci. Rep., 8, 13952, https://doi.org/10.1038/s41598-018-32339-9, 2018.

Ritter, B., Wennrich, V., Medialdea, A., Brill, D., King, G., Schneiderwind, S., Niemann, K., Fernández-Galego, E., Diederich, J., Rolf, C., Bao, R., Melles, M., and Dunai, T. J.: Climatic fluctuations in the hyperarid core of the Atacama Desert during the past 215 ka, Sci. Rep., 9, 5270, https://doi.org/10.1038/s41598-019-41743-8, 2019.

Ritter, B., Vogt, A., and Dunai, T. J.: Technical Note: Noble gas extraction procedure and performance of the Cologne Helix MC Plus multi-collector noble gas mass spectrometer for cosmogenic neon isotope analysis, Geochronology, 3, 421–431, https://doi.org/10.5194/gchron-3-421-2021, 2021.

Ritter, B., Diederich-Leicher, J. L., Binnie, S. A., Stuart, F. M., Wennrich, V., Bolten, A., and Dunai, T. J.: Impact of $CaSO_4$-rich soil on Miocene surface preservation and Quaternary sinuous to meandering channel forms in the hyperarid Atacama Desert, Sci. Rep., 12, 17951, https://doi.org/10.1038/s41598-022-22787-9, 2022.

Roldán, F., Salazar, I., González, G., Roldán, W., and Toro, N.: Flow-Type Landslides Analysis in Arid Zones: Application in

La Chimba Basin in Antofagasta, Atacama Desert (Chile), Water, 14, 2225, https://doi.org/10.3390/w14142225, 2022.

Sáez, A., Cabrera, L., Garcés, M., van den Bogaard, P., Jensen, A., and Gimeno, D.: The stratigraphic record of changing hyperaridity in the Atacama desert over the last 10 Ma, Earth Planet. Sc. Lett., 355, 32–38, https://doi.org/10.1016/j.epsl.2012.08.029, 2012.

Sáez, A., Godfrey, L. V., Herrera, C., Chong, G., and Pueyo, J. J.: Timing of wet episodes in Atacama Desert over the last 15 ka. The Groundwater Discharge Deposits (GWD) from Domeyko Range at 25° S, Quat. Sci. Rev., 145, 82–93, https://doi.org/10.1016/j.quascirev.2016.05.036, 2016.

Sager, C., Airo, A., Arens, F. L., and Schulze-Makuch, D.: New type of sand wedge polygons in the salt cemented soils of the hyper-arid Atacama Desert, Geomorphology, 373, 107481, https://doi.org/10.1016/j.geomorph.2020.107481, 2021.

Scheuber, E. and Andriessen, P. A. M.: The kinematic and geodynamic significance of the Atacama fault zone, northern Chile, J. Struct. Geol., 12, 243–257, https://doi.org/10.1016/0191-8141(90)90008-M, 1990.

Stern, C. R.: Active Andean volcanism: its geologic and tectonic setting, Rev. Geol. Chile, 31, 161–206, 2004.

Sun, T., Bao, H., Reich, M., and Hemming, S. R.: More than ten million years of hyper-aridity recorded in the Atacama Gravels, Geochim. Cosmochim. Ac., 227, 123–132, https://doi.org/10.1016/j.gca.2018.02.021, 2018.

Voigt, C., Klipsch, S., Herwartz, D., Chong, G., and Staubwasser, M.: The spatial distribution of soluble salts in the surface soil of the Atacama Desert and their relationship to hyperaridity, Global Planet. Change, 184, 103077, https://doi.org/10.1016/j.gloplacha.2019.103077, 2020.

Wagner, G. A.: Age Determination of Young Rocks and Artifacts: Physical and Chemical Clocks in Quaternary Geology and Archaeology, Springer Berlin Heidelberg, Berlin, Heidelberg, 466 pp., https://doi.org/10.1007/978-3-662-03676-1, 1998.

Wennrich, V., Böhm, C., Brill, D., Carballeira, R., Hoffmeister, D., Jaeschke, A., Kerber, F., Maldonado, A., May, S. M., Olivares, L., Opitz, S., Rethemeyer, J., Reyers, M., Ritter, B., Schween, J. H., Sevinç, F., Steiner, J., Walber-Hellmann, K., and Melles, M.: Late Pleistocene to modern precipitation changes at the Paranal clay pan, central Atacama Desert, Global Planet. Change, 233, 104349, https://doi.org/10.1016/j.gloplacha.2023.104349, 2024.

Wennrich, V., Diederich-Leicher, J., and Ritter, B.: Supplement to "Unearthing the climate history of the Atacama Desert in northern Chile – deep drilling in two clay pans of the Coastal Cordillera", Collaborative Research Centre 1211 – Database [data set], https://www.crc1211db.uni-koeln.de/search/view.php?dataID=1031 (last access: 7 July 2025), 2025.

Yogeshwar, P., Küpper, M., Tezkan, B., Rath, V., Kiyan, D., Byrdina, S., Cruz, J., Andrade, C., and Viveiros, F.: Innovative boat-towed transient electromagnetics – Investigation of the Furnas volcanic lake hydrothermal system, Azores, Geophysics, 85, E41–E56, https://doi.org/10.1190/geo2019-0292.1, 2020.

Zander, A. and Hilgers, A.: Potential and limits of OSL, TT-OSL, IRSL and $pIRIR_{290}$ dating methods applied on a Middle Pleistocene sediment record of Lake El'gygytgyn, Russia, Clim. Past, 9, 719–733, https://doi.org/10.5194/cp-9-719-2013, 2013.

Zinelabedin, A., Mohren, J., Wierzbicka-Wieczorek, M., Dunai, T. J., Heinze, S., and Ritter, B.: Haloturbation in the northern Atacama Desert revealed by a hidden subsurface network of calcium sulfate wedges, Earth Surf. Dynam., 13, 257–276, https://doi.org/10.5194/esurf-13-257-2025, 2025.